IMPROVING VEGETATION AND BACKGROUND DISCRIMINATION FROM HYPERSPECTRAL IMAGING (HSI) AND LIGHT DETECTION AND RANGING (LIDAR) FUSION USING AN ADDED SHORTWAVE INFRARED (SWIR) HSI COMPONENT

by

Joshua F. Magarick
A Thesis
Submitted to the
Graduate Faculty
of
George Mason University
in Partial Fulfillment of
The Requirements for the Degree
of
Master of Science
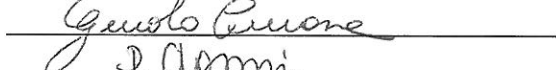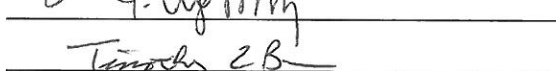Geoinformatics and Geospatial Intelligence

Committee:

_____ Dr. Tony Stefanidis, Thesis Director

_____ Dr. Ronald G. Resmini, Committee Member

_____ Dr. Guido Cervone, Committee Member

_____ Dr. Peggy Agouris, Department Chair

_____ Dr. Timothy L. Born, Associate Dean for Student and Academic Affairs, College of Science

_____ Dr. Vikas Chandhoke, Dean, College of Science

Date: 15 November 2012   Fall Semester 2012
George Mason University
Fairfax, VA

Improving Vegetation and Background Discrimination from Hyperspectral Imaging (HSI) and Light Detection and Ranging (LiDAR) Fusion Using an Added Shortwave Infrared (SWIR) HSI Component

A thesis submitted in partial fulfillment of the requirements for the degree of Master of Science at George Mason University

by

Joshua F. Magarick
Bachelor of Arts
University of Colorado at Boulder, 2004

Director: Tony Stefanidis, Professor
Department of Geoinformatics and Geospatial Intelligence

Fall Semester 2012
George Mason University
Fairfax, VA

DEDICATION

To those who seek broad scientific advancements in the field of Imaging Spectroscopy.

ACKNOWLEDGEMENTS

TABLE OF CONTENTS

LIST OF TABLES

LIST OF FIGURES

LIST OF EQUATIONS

LIST OF ABBREVIATIONS AND SYMBOLS

Airborne Imaging Spectrometer for Applications .... AISA
Airborne Visible / Infrared Imaging Spectrometer .... AVIRIS
Above Ground Level.. AGL
Area of Interest .... AOI
Area Under the Curve .... AUC
Atmospherically Resistant Vegetation Index...ARVI
Boise Center for Aerospace Laboratory ....BCAL
Canopy Height Model... CHM
Cellulose Absorption Index ....CAI
Compact Airborne Spectrographic Imager .... CASI
Digital Canopy Model... DCM
Digital Elevation Model...DEM
Digital Terrain Elevation Data..DTED
District of Columbia Geographic Information System...DC GIS
Geographic Information System .... GIS
Ground Control Point...GCP
Ground Sampling Distance ....GSD
Hue, Saturation, and Value ....HSV
Hyperspectral Imaging... HSI
Imaging Spectroscopy..IS
Input Geometry ....IGM
Infrared...IR
Jet Propulsion Laboratory .... JPL
Kilohertz ....kHz
Light Detection and Ranging ....LiDAR
Longwave Infrared.. LWIR
Meters .... M
Matched Filter...MF
Maximum Likelihood Classifier..MLC
Minimum Noise Fraction..MNF
Mixture Tuned Matched Filter...MTMF
Moisture Stress Index .... MSI
Near Infrared...NIR
Normalized Difference Infrared Index..NDII
Normalized Difference Vegetation Index...NDVI
Principal Component ....PC

ABSTRACT

IMPROVING VEGETATION AND BACKGROUND DISCRIMINATION FROM
HYPERSPECTRAL IMAGING (HSI) AND LIGHT DETECTION AND RANGING
(LIDAR) FUSION USING AN ADDED SHORTWAVE INFRARED (SWIR) HSI
COMPONENT

Joshua F. Magarick, M.S.

George Mason University, 2012

Thesis Director: Dr. Tony Stefanidis

An observation made with respect to reviewing previous work in this domain is

that many authors do not include the use of shortwave infrared (SWIR) bands that are

made available by some hyperspectral imaging (HSI) sensor systems. This work will

investigate the fusion of HSI and light detection and ranging (LiDAR) data that will

include the use of SWIR bands during the fusion process in order to better characterize,

discriminate, map, detect, and possibly identify, background vegetation materials. Data

for this project comes from an August 2008 collection over the Washington, DC National

Arboretum using the Mapping Reflected Energy Spectrometer (MaRS) Visible Near

Infrared and SWIR (VNIR/SWIR) HSI system, and also from an Optech 3100 ALTM

LiDAR system. The two targets chosen for analysis were the American sweetgum tree

and several trails (footpaths). The objective of this work is to run several data fusion

experiments where LiDAR raster transformations are fused with VNIR-only, SWIR-only, and full VNIR/SWIR HSI data to investigate which combination of fusion methods are optimal under the given circumstances. In some cases, improvement in the American sweetgum tree detection and trails detection is noted when the SWIR HSI bands are included in the data fusion analysis.

INTRODUCTION

Hyperspectral Imagery ─ HSI

It is widely known that plenty of work has been completed within the domain of HSI and LiDAR data fusion for different purposes such as geologic mapping, riparian vegetation mapping, tropical vegetation mapping and discrimination, low lying grass, bush, and brush discrimination, and complex forest area classifications [49][23][4][31][14]. HSI is also commonly referred to as imaging spectroscopy (IS). IS, as defined by Goetz et al. (1985), is based on sensors that have the ability to simultaneously collect data using a large number─often hundreds─of narrow spectral bands over a continuous range of the electromagnetic spectrum [21]. Something less commonly discussed regarding HSI is that it is not necessarily a requirement that HSI sensors have more than one hundred bands; rather, it often may depend on a specific problem set of the end-user. For example, consider a material that has only two spectral features of interest that each span 0.05µm. Perhaps a system with only 40 spectral bands that covers each of these features─depending on the width and depth of those features─could be considered an HSI system just so long as the material in question can be properly detected using such band assignments. Moreover, the spectral range of IS is certainly not limited to the VNIR/SWIR (0.4 µm - 2.5 µm) spectral range; rather, it has also been demonstrated as useful in the midwave infrared (MWIR) range (3.0 µm - 5.5 µm) and also the longwave infrared (LWIR) range (7.5 µm - 13.5 µm) [22][46].

Historically, the VNIR range has been shown to be particularly useful for vegetation

discrimination, while the SWIR has been particularly useful in geologic material

discrimination [1] [29]. With regards to the HSI data analyzed here, the intention of this

topic will be to cover as much of the VNIR/SWIR range as possible (less those bands

where the atmosphere does not transmit signal and that contain unacceptable levels of

noise due to system constraints) for the purposes of vegetation discrimination and

background identification and/or suppression.

LiDAR

LiDAR is more straightforward and thus slightly easier to describe. LiDAR is an

active system that fires a laser pulse with a specific narrow wavelength [48]. Although

there are some minor variations, common active LiDAR system laser wavelengths

include the visible green 0.532 µm, and the infrared (IR) wavelengths of 1.064 µm and

1.550 µm. Although seemingly instantaneous, a laser travels at the speed of light, which

can be measured. The time it takes for the laser pulse to reach the ground (or object—not

all LiDAR systems are airborne) and return to the system can be calculated. As long as

the altitude and position of the aircraft is well known, differences in the measured times

of each laser return are used to precisely calculate ground elevations. The number of

points, density of points, and accuracy of elevation is determined by the particular make

and model of LiDAR system in operation. It is also understood that the original priority

of LiDAR was to only generate high resolution digital elevation models (DEMs) [48].

When a laser pulse is transmitted from a LiDAR system, it can, depending on the spot

size of the laser once it reaches the ground, produce multiple returns which can result in

LiDAR pulses reaching both the ground (second return), and an object above the ground (first return), such as a tree limb. In order to generate a DEM, the first return LiDAR points are simply thrown out if they are considered above the ground thus allowing the user to produce DEMs of only the bare earth. It was found that, by keeping first return LiDAR points on those objects such as trees, three dimensional (3D) models of these above-ground objects could also be produced. Additionally, LiDAR systems that can achieve higher point densities per square meter (m^2) will likely have higher rates of return on bare earth and objects of interest. For example, according to Li et al. (2012) [30], tree structures maybe better modeled with higher point density LiDAR systems since there would be a higher probability of laser pulses penetrating tree-top canopies to reach parts of the tree (limbs, branches) under the top canopy, and eventually the ground. Moreover, Asner et al. (2007) [5] state that high LiDAR pulse repetition rates of 70 - 100 kHz will have a better chance at foliage penetration to the ground, which would in turn produce better overall canopy characterization.

HSI and LiDAR Fusion for Vegetation

Although previous studies have been conducted, the mapping and discrimination of different vegetation types using HSI and LiDAR fusion remains an activity in which further development is warranted. While some analysis methods such as onboard HSI-LiDAR hardware mounting and software-based feature and pixel fusion have been presented, no single fusion method has become widely accepted as a standard by the HSI and LiDAR communities [49][4][31][14][30][5]. The importance of using HSI and LiDAR fusion for vegetation mapping has been highlighted in multiple studies. Some of

these reasons include floodplain vegetation mapping for the purposes of studying the role vegetation has on hydraulic resistance, forest preservation and management, detecting, identifying, and mapping invasive species to a particular biome, and mapping certain types of vegetation for the purposes of forest fire preparation planning and management [20][14][4][27]. Asner et al. (2008) [4] and Jones et al. (2010) [25] are examples of two studies that have published HSI and LiDAR fusion materials that also take some of the SWIR bands into consideration. Asner et al. (2008) [4] use these bands to estimate live and dead vegetation cover using Airborne Visible Infrared Imaging Spectrometer (AVIRIS) VNIR/SWIR HSI data while Jones et al. (2010) [25] use a small subset of SWIR bands for continued vegetation discrimination—as opposed to additional background characterization—that go out to ~2.40 µm. Neither of these authors, however, specifically evaluated the use of VNIR-only, SWIR-only, or full VNIR/SWIR HSI and LiDAR fusion in their work.

Two other authors, Schmidt and Skidmore (2002) [40], show–using statistical analysis of field and lab spectra of vegetation–how various parts of the VNIR/SWIR portion of the spectrum contribute to vegetation discrimination. In particular, they discuss portions of the SWIR–in addition to the near infrared (NIR)–that can maximize the discrimination of vegetated species. Based on the work of Schmidt and Skidmore (2002) [40], as well as the community's preference for leaving out the SWIR, it is sensible to test the addition of SWIR bands for this HSI and LiDAR fusion project.

Another key point to add is that this work involves the undertaking of one of the more difficult problems in this field: mapping and attempting to discriminate certain

types of vegetation using small target datasets contained within a predominately vegetated background. Ribeiro and Crowley (2010) [36] use LWIR HSI data to map some types of vegetation around the State Arboretum of Virginia (not to be confused with the National arboretum referred to in this work). Although Ribeiro and Crowley (2010) [36] do not use VNIR/SWIR HSI and do not include LiDAR in their work, their data collection parameters and objectives were similar to the work herein- discriminating vegetation using small target datasets that contain primarily vegetation in the scenes. In their conclusions, Ribeiro and Crowley (2010) [36] state that better atmospheric compensation and improved spectral analysis methods will be needed in order to harness the full potential of such LWIR HSI datasets for mapping vegetation. Perhaps the addition of LiDAR fused with LWIR could be one way of enhancing their analysis.

The bulk of the literature and background review that will be covered below discusses specific topics related to the fusion of HSI and LiDAR data for vegetation mapping and discrimination. The work presented here will expand upon the principles of exploiting SWIR data─fused with LiDAR data─in order to characterize, and thus discriminate and possibly identify, background materials surrounding vegetation during the trails analysis. Additionally, vegetation discrimination will be demonstrated using HSI fused with some of the numerous raster outputs of LiDAR including vegetation height statistics and vegetation roughness estimations for the American sweetgum analysis.

LITERATURE REVIEW AND CURRENT STATE-OF-THE-ART

VNIR HSI and LiDAR Fusion

There are several key papers that will be reviewed in this thesis, and also continuously cited throughout. Geerling et al. (2007) [20] is an example of one such study. They discuss many of the fusion methodologies that were applied throughout this thesis. Unlike other authors, they clearly point out the three overall levels of data fusion: decision level, feature level, and pixel level that were also discussed by Pohl and van Genderen (1998) [35]. Decision level fusion, with respect to geoprocessing, is a high level of data fusion that occurs when the results of georegistered datasets are brought together only after such data have been processed in separate software packages. A typical example would include a Quickbird image orthorectified using Overwatch's RemoteView™ Electronic Light Table (ELT) [33]. The post processed, orthorectified Quickbird image could then be draped onto a corresponding high resolution LiDAR DEM using ESRI's ArcScene™ [16] software where the LiDAR data are preprocessed using Applied Imagery's Quick Terrain (QT) Modeler™ [2] software. Geospatial analysis using the three-dimensional (3D) capabilities of ArcScene™ could be completed thereafter, which is an example of decision level fusion. Feature level fusion also involves the processing of data sources in multiple software packages where objects such as shapefiles are extracted from each data source and then used for additional tipping and queuing of each data source to find additional targets or areas of interest (AOIs). Lastly,

the pixel level fusion of two datasets, such as HSI and LiDAR, involves the immediate

fusion of properly coregistered pixels from each data source. An example of this in the

context of HSI and LiDAR fusion would be using LiDAR generated and rasterized digital

canopy models (DCMs) and surface roughness rasters stacked into a file containing

multiple bands derived from HSI processing using the ENVI® [18] software. This single,

coregistered, multi-banded file could then be processed using standard algorithms such as

a mixture tuned matched filter (MTMF) [10] or an adaptive coherence estimator (ACE)

[28]. This type of pixel level fusion is similar to that of Geerling et al. where vegetation

discrimination using HSI and LiDAR fusion was demonstrated in the Netherlands [20].

Geerling et al., however, only used 10 bands of the airborne HSI CASI data, and did not

have access to SWIR data. It is stated in the paper that there was some level of difficulty

when attempting to separate bare soil from low lying grasslands using the HSI and

LiDAR. Although the single band of 3D LiDAR data would be a good discriminator for

areas that are generally low lying and thus may not be vegetated, it would not be able to

identify whether these low lying areas (i.e. completely flat areas such as bare soil or

tramped footpaths where the height above ground is less than 10 cm) were comprised of

vegetation or bare soil. Even though some idea of bare earth type may be obtained using

only 10 VNIR CASI bands, it would have been much more useful to have included SWIR

bands in this analysis as well.

Mundt et al. (2006) [31] also use VNIR HSI data collected with the airborne

HyVista system in conjunction with LiDAR data to improve the results of sagebrush

classification in Idaho. Although the HyVista system covers the full VNIR/SWIR (0.4

7

μm - 2.5 μm) spectral range, the authors chose to only use a subset of the VNIR portion

of the spectrum (0.605 μm - 0.984 μm), which only consisted of 27 spectral bands after

band subsetting. The authors state that the amount of sagebrush vegetation was sparse in

the study area, which made this type of vegetation easy to separate from the background

using MTMF as the means of analyzing the HSI data. It appears that they chose to

eliminate the SWIR portion of the spectrum for two reasons. First, when using the full

VNIR/SWIR spectral range, it was noted that MTMF would overestimate the amount of

sagebrush due to burned areas as a result of previous wild fires in the study area. Second,

it was claimed that the use of the full VNIR/SWIR range resulted in generally confused

classification results due to bright soil backgrounds that are not easily discriminated.

There seemed to be two factors the LiDAR proved extremely useful for here. First was

classifying the LiDAR into ground or non-ground points (i.e., calculating a DCM-

sometimes also referred to as a canopy height model). The height model was used for

obvious discrimination of whether sagebrush was present; sagebrush does not grow high

above the surface, and thus, taller objects—those above 1 m—could be negated. The

second raster made possible by LiDAR was the surface roughness calculation. The

authors looked at this raster multiple times to determine what surface roughness (the

standard deviation of above ground elevation values) values best matched that of

sagebrush. Smooth surfaces were often the result of manmade features such as roads

while rough and tall features were also the result of other manmade objects such as utility

poles. Roughness threshold values were determined that were used to indicate either the

presence or absence of sagebrush. If a separate pre-processing of only the SWIR data

were executed in addition to the VNIR processing, additional separability from the soil background could have been achieved, especially if using the spectral features pointed out by Asner et al. (2007) [5]. Perhaps this additional SWIR data processing could have resulted in a raster dataset that might have been included in the final MTMF-versus-roughness scatter plot shown in the paper as a third dimension to further negate false alarms.

Current State-of-The-Art HSI and LiDAR Fusion

Asner et al. (2007) [5] have completed the most extensive work to date that incorporates SWIR bands into the HSI and LiDAR fusion analysis process. In this paper, an auto Monte Carlo unmixing (Auto-MCU) approach was used on the HSI data with so-called tied-SWIR, which is described in a separate paper by Asner et al. (2002) [3]. The tied-SWIR is a means of subtracting a reflectance value from one wavelength (the tie point) from all other bands [3]. The tied-SWIR method is beneficial because it is not as sensitive to finer noise bands. Moreover, Asner et al. (2002) [3] show that the use of tied-SWIR spectra, similar to first derivative spectra, improves the user's ability to distinguish features that are characteristic of specific endmembers, and especially those endmembers in the SWIR that relate to bare soil or bare substrates. This would be an interesting concept if applied to manmade materials or other geologic materials, and warrants further investigation. Nevertheless, Asner et al. (2007) [5] used tied-SWIR to separate photosynthetic vegetation (PV) from non-photosynthetic vegetation (NPV) and to detect bare substrate between these vegetation types. It should be noted that although these authors have introduced and chosen the tied-SWIR method to accomplish this analysis,

this is certainly not the only way to achieve these types of results while incorporating the SWIR; for example, Jones et al. (2010) [25] used a support vector machine (SVM) to incorporate similar bands into their analysis. Pixel maps are generated that demonstrate their final results using both the HSI and LiDAR data collected during their experiment [5]. LiDAR data was initially used to calculate ground terrain (i.e., a DEM) and vegetation canopy surface. These calculations lead to the ability to calculate vegetation height and shape. With vegetation height and shape already calculated using the LiDAR data; they could then determine areas where shadows may exist with respect to sun angle and azimuth. Shadows are not an issue for the LiDAR system since it uses an active illumination source—the laser; rather, shadows are an issue for the HSI system, which is a passive instrument, and uses the sun as the primary illumination source. By determining areas that would be affected by shadows using the LiDAR data, such areas could be masked during HSI data analysis. Jones et al. (2010) [25] have used both feature level fusion, and pixel level fusion in their analysis—as defined by Pohl and van Genderen, (1998) [35]. Asner et al. (2007) [5] and Geerling et al. (2007) [20] provide examples of feature level fusion where areas found to contain shadows calculated in the LiDAR data are later used to masked areas in the HSI data. Pixel level fusion appears to occur in the final invasive species detection planes, which are shown in the paper. One other note is that the data used by Asner et al. (2007) [5] were collected over Hawaiian rainforests and apparently did not take into account any manmade obstacles or materials such as roads or buildings. Through many of their papers, Asner et al. have not only incorporated the

SWIR, but have also demonstrated what is perhaps the state-of-the-art in the field of HSI and LiDAR fusion for vegetation analysis.

A study by Brook et al. (2010) [12] also demonstrates the use of HSI and LiDAR fusion using full VNIR/SWIR Airborne Imaging Spectrometer for Applications (AISA) data. Interestingly, the data used is somewhat analogous to the data used in this thesis; full VNIR/SWIR HSI data, and LiDAR data collected at 1.050 μm (a slightly different laser wavelength) at 100 kHz [12]. The authors do not state the exact LiDAR system used for their work. Brook et al. (2010) [12] make two well stated points in their paper. First, they state that both spectral and 3D spatial information are needed for comprehensive real-time analysis of urban environments [12]. Second, they state that the surface composition of urban materials can be identified by spectral analysis while being coincidentally mapped using LiDAR data in 3D visualizations [12]. They then assert that chemical runoff (i.e., from pollutants) detected using HSI could be mapped in this 3D environment as well [12]. Although Brook et al. (2010) [12] use the full spectral range to detect scene endmembers using the HSI data; they do not identify the endmembers that they detect. It is clear that the scene used for analysis contains manmade materials such as asphalt and tile roofs, and also natural background materials such as gravel and soils, but these could be identified by general photo interpretation. The authors have probably detected these endmembers using the pixel purity index (PPI) algorithm [9] followed by mapping with the spectral angle mapper (SAM) algorithm, but do not identify these materials in the final product [12]. The means of data coregistration and fusion between the HSI and LiDAR involves a scene-to-scene feature based method where edges are

automatically aligned between the two datasets [12]. Although the registration between the two datasets looks good, the authors do not provide a quantitative pixel-based measure of exactly how good the feature-based registration is between the two datasets (i.e., within a pixel, two pixels, etc). In general, it would be more beneficial to have the final products presented using some standard cartographic principles such as including a legend, scale, north arrow, and stating the general geographic location on the product (the nation of Israel in this case).

The study by Onojeghuo and Blackburn (2011) [32] discussed the use of full VNIR/SWIR HSI data and LiDAR fusion for mapping areas containing reedbeds. Reeds are generally described as tall grasses that surround wetland areas, while reedbed describes an entire landscape of such grasses [32]. Similar to Brook, et al. (2010) [12], Onojeghuo and Blackburn (2011) [32] also use a similar HSI and LiDAR system setup that is analogous to those systems used for this thesis project. Onojeghuo and Blackburn (2011) [32] used the AISA Eagle and AISA Hawk systems, which collected VNIR and SWIR HSI data coincidentally. Moreover, a Leica ALS50 collected LiDAR coincidentally with the HSI using a laser with a wavelength of 1.064 μm at a pulse rate of 83 kHz. Onojeghuo and Blackburn (2011) [32] state that the LiDAR point density was 3.5 points per m^2. The maximum pulse rate of 83 kHz of the Leica ALS50 system could have slightly limited the overall point density; Optech LiDAR systems are able to collect at pulse rates of 100 kHz or even higher. Onojeghuo and Blackburn (2011) [32] are the only authors that seem to deliberately breakdown the results of using VNIR versus SWIR HSI, and both combined, in combination with LiDAR to map vegetation (reedbeds). For

the purposes of mapping reedbeds, the authors came to the conclusion that using only the

VNIR portion of the spectrum fused with a height mask derived from the LiDAR data

produced the best results. The authors claimed that incorporating the SWIR only included

redundant data, and that the inclusion of redundant data (i.e., input of SWIR bands)

reduced the overall accuracy of the classification [32]. Another important point to note

here is that Onojeghuo and Blackburn only chose to use the LiDAR as a height mask and

nothing more. They attempted to fuse the LiDAR-derived CHM band directly into the

HSI data as an additional band (i.e., layer stacking), but this drastically reduced the

accuracy of the classification. Consequently, they derived a height mask from the LiDAR

data, and applied this to the HSI data prior to classification in order to improve the

overall results of the classification [32]. Other authors, such as Jones, et al. (2010) [25],

obtained similar results when using LiDAR as a height mask. What is surprising,

however, is that Onojeghuo and Blackburn (2011) [32] did not attempt to derive surface

roughness using the LiDAR data; rather, they only derived surface roughness from the

HSI data using texture co-occurrences. It seems that deriving surface roughness of the

reedbeds from the LiDAR data, (similar to Mundt et al. (2006) [31], and West and

Resmini, (2009) [49]), and fusing this information with the HSI data would improve the

classification accuracy of the reedbeds even more. Another unforeseen aspect of

Onojeghuo and Blackburn's paper is that a maximum likelihood classifier (MLC) was

used in conjunction with the HSI data to assist in the mapping of the reedbed vegetation.

It should be noted that most other authors choose to use other types of classifiers.

Geerling et al. is the only other author reviewed that─when carrying out work in HSI and

LiDAR fusion—used the MLC as the primary classifier for the HSI data [20]. Asner et al. (2007) [5] used the tied-SWIR method. Dalponte et al. (2009) [14], Jones et al. (2010) [25], and Koetz et al. (2008) [27] each chose to use the SVM method. Dalponte et al. (2009) [14] and Jones et al. (2010) [25] each specify that the MLC method is not a robust method of classification. Salvador and Resmini (2009) [49] chose to evaluate several types of classifiers to include the MF, SAM, and linear unmixing. Mundt et al. (2006) [31] and Sankey and Glenn (2011) [39] each chose the MTMF to map vegetation using HSI data. Onojeghuo and Blackburn (2011) [32] chose to use the MLC for two reasons. First, they claim that it is a robust algorithm and that it has been shown to perform well for the purposes of mapping vegetation, and second, it is widely available in most commercial software packages at no charge [32]. Nevertheless, this use of a wide variety of classifiers demonstrates that authors have been successful using many types of techniques, but that most authors believe the MLC is a dated method. The best approach maybe to test several classification methods based on the problem set at hand.

Previous Work on MaRS HSI and LiDAR Fusion

To date, there are three known published papers that involve the use of MaRS data, and the MaRS sensor generally. One of these papers, by West and Resmini (2009) [49] involves the use of HSI and LiDAR fusion specifically for a geological analysis of Cuprite, Nevada. The authors use standard HSI filtering techniques such as matched filtering and linear spectral mixture analysis to identify the local geology such as kaolinite and alunite. Using coincidentally collected LiDAR data, surface roughness of the area was calculated. The authors attempted to find a correlation between surface

roughness and geology types. Although it is believed that there might be some small correlation, it is thought that the LiDAR GSD of approximately 1 m was too large to make accurate assessments of geology and mineralogy surface roughness. The idea of visually interpreting LiDAR surface roughness against HSI filtering techniques was successfully used to map sagebrush in Idaho, but the surface roughness of rocks is much finer than that of vegetation and would thus require LiDAR data with more resolution [31]. Regarding West and Resmini (2009) [49], one item to point out includes the aircraft flying underneath a cloud deck on the day of the data collection. Although flying underneath a cloud deck would not affect an active LiDAR system, it would most certainly negatively impact a passive VNIR/SWIR HSI system such as MaRS. In particular, the SWIR region would be most affected since, according to Simi and Reith (2009) [42], there tends to be less signal in the SWIR portion of the MaRS and AVIRIS VNIR/SWIR HSI systems than in the VNIR. As a side note, it should be made apparent that, although Simi and Reith call the system the "Mapping Reflected energy Sensor," this system has since been commonly referred to as the "Mapping Reflected energy *Spectrometer*." Even though West and Resmini (2009) [49] present a custom method for atmospheric correction, and mineral maps appear accurate according to ground truth, there are no spectra shown in the paper to verify the results of the custom atmospheric correction method presented. Lastly, it should also be noted that few words are stated with respect to the preprocessing of the MaRS data such as which bands were eliminated as "bad" during the processing. Knowledge of which band specific regions were used for their analysis would be useful for determining how they came to these conclusions. It is

important to note here that the SWIR region was used as the primary spectral discriminator for mineralogy, and was later fused with the LiDAR data. This thesis will potentially use some of the spectral filtering techniques presented here, and from Asner et al. (2000) [3], to assist in additional vegetation and background discrimination.

In a paper by Salvador and Resmini (2009) [38], the MaRS data were analyzed with respect to what spectral matching techniques might be most useful for vegetation discrimination using MaRS data over the National Arboretum[38]. The HSI data presented in Salvador and Resmini (2009) [38] is the same HSI data that will be used for this thesis. Salvador and Resmini did not use the LiDAR data that were also collected coincidentally with the HSI over the Arboretum. Moreover, they focused specifically on the use of the VNIR/SWIR data for vegetation discrimination, and only used a Normalized Difference in Vegetation Index (NDVI) for masking out areas that were not vegetated. Some of the spectral mapping methods that Salvador and Resmini applied to the Arboretum such as Matched Filtering, 1st derivative filtering, and MTMF may be used during both the spectral analysis and pixel level HSI and LiDAR fusion portion of this thesis.

DATA & STUDY SITE

Data for this project comes from the MaRS VNIR/SWIR HSI system and the Optech ALTM 3100 LiDAR system. Both systems were mounted coincidentally onboard a C-131 aircraft. Photos and ground truth of the National Arboretum study site will also be presented in this section.

MaRS (HSI)

The MaRS system, developed by the Jet Propulsion Laboratory (JPL), is similar in specifications to AVIRIS, also developed by JPL. It nominally collects 332 bands of spectral data between 0.38 μm and 2.515 μm with a spectral resolution of 4 nm in the VNIR and 8 nm in the SWIR [42]. It should be noted that there is a focal plane overlap region between the two 640x480 pixel VNIR and SWIR focal planes [42]. This overlap region occurs between approximately 0.800 μm and 0.825 μm and corresponds to spectral band numbers 112 − 121; these are typically the first bands that are eliminated and considered bad bands by the user. Additionally, there is a slight, 40 pixel, physical gap between the two focal planes. Thus, although the raw data files are 640 pixels wide, the VNIR and SWIR bands are brought together (i.e., coregistered) automatically during the calibration process provided by JPL. This process leaves 15 samples of zero value data on the left side of the data cubes and 25 samples of zero value data on the right side

of the cubes. These samples must be removed (i.e., subsetted), which leaves the user with 600 samples of useable data. Under optimal conditions such as proper aircraft altitude, data sampling speed, aircraft speed, and weather conditions, the MaRS system is capable of a high signal-to-noise ranging from 1200 – 1800 [42].

For this data collection on August 12th, 2008, over the National Arboretum, a total of nine flight lines were collected with ground sampling distances (GSD) ranging between approximately 0.67 meters and 0.76 meters. For the purposes of this thesis, only 4 of the flight lines were chosen, and only two of them will be utilized. Near infrared composites of MaRS lines collected of the National Arboretum used for this project are shown in Figure 1 through Figure 4. Additionally, panchromatic LiDAR data (shown as intensity images) that were collected coincidentally with the MaRS HSI data are shown alongside the MaRS images.

Optech ALTM 3100 (LiDAR)

The Optech ALTM 3100 LiDAR system operates with a laser at 1.064 μm and collects data at a frequency of 100 kHz. During preprocessing, it was found that the point density of the LiDAR data over the National Arboretum ranges, on average, from 6.67 points per m^2 to 10.51 points per m^2. Precise measures of LiDAR point density are outlined in Table 2. Although LiDAR data were collected coincidentally with the MaRS HSI data onboard the same aircraft, the swath width of the LiDAR data is different than that of the MaRS data. It should be noted that there are also differences in the GSD of the HSI and LiDAR systems. The GSDs and aircraft altitudes given in Table 1 are approximate. Due to slight variations in aircraft altitude during flight and also minor

variations in ground elevation throughout each of the scenes, there can be GSD variations

on the order of ±5%. Nevertheless, HSI data will be interpolated to that of the slightly

lower overall resolution LiDAR data of 1 m. This process is accomplished using the

ENVI® software, which uses a nearest neighbor interpolation. Initial tests using this

method between HSI and LiDAR datasets showed quite good results.
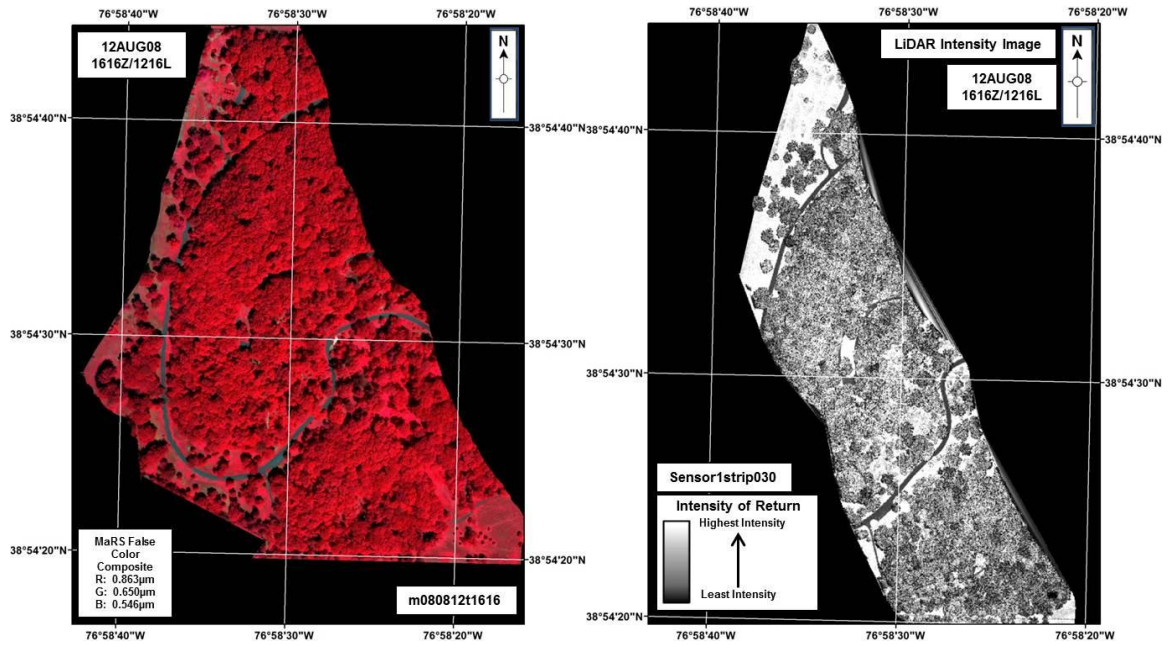
Figure 1: MaRS NIR Composite (left) and Optech ALTM 3100 LiDAR Intensity Image (right) of the National Arboretum, Washington, DC. In the MaRS NIR composite, the red band is displayed as 0.863 μm, green 0.650 μm, and blue 0.546 μm. Both data files have been projected to UTM Zone 18 North, and the datum used is the North American Datum 1927 (NAD27). Collection time 1616Z.
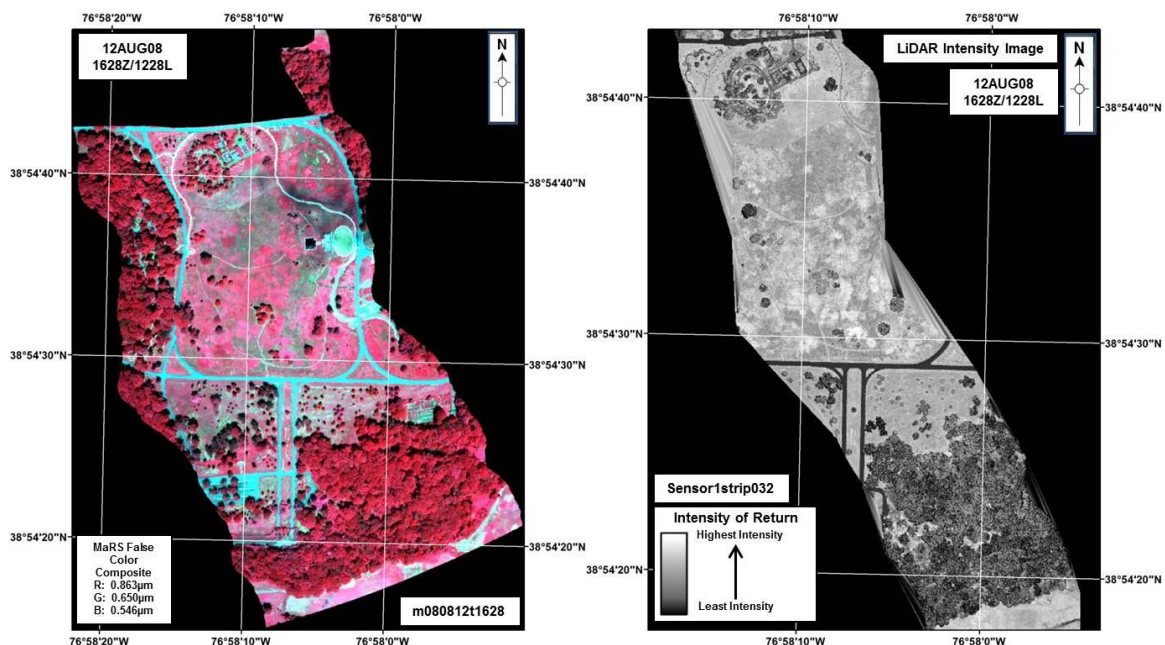
Figure 2: MaRS NIR Composite (left) and Optech ALTM 3100 LiDAR Intensity Image (right) of the National Arboretum, Washington, DC. In the MaRS NIR composite, the red band is displayed as 0.863 µm, green 0.650 µm, and blue 0.546 µm. Both data files have been projected to UTM Zone 18 North, and the datum used is the North American Datum 1927 (NAD27). Collection time 1628Z.

Table 1: HSI and LiDAR data used for this project. The aircraft altitude was measured in feet above ground level (AGL). The ground sampling distances (GSD) represent the size of a single pixel as it represents the ground from each system.

| 12 August 2008 - Washington, DC National Arboretum Coincident HSI & LiDAR Data Collection					
Time (Zulu)	Altitude (Feet - AGL)	LiDAR GSD (m)	HSI GSD (m)	LiDAR File Name	HSI File Name
1616	2500	1	0.76	Sensor1strip030.las	m080812t1616
1628	2500	1	0.75	Sensor1strip032.las	m080812t1628
1644	2500	1	0.67	Sensor1strip035.las	m080812t1644
1659	2500	1	0.67	Sensor1strip038.las	m080812t1659

20
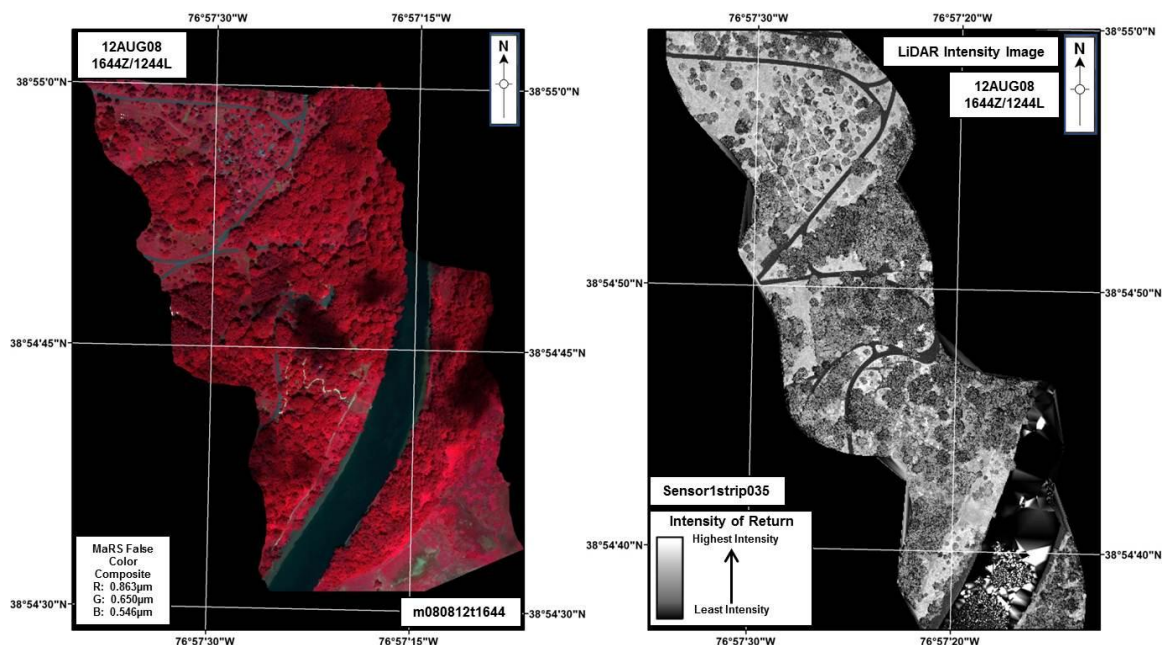
Figure 3: MaRS NIR Composite (left) and Optech ALTM 3100 LiDAR Intensity Image (right) of the National Arboretum, Washington, DC. In the MaRS NIR composite, the red band is displayed as 0.863 μm, green 0.650 μm, and blue 0.546 μm. Both data files have been projected to UTM Zone 18 North, and the datum used is the North American Datum 1927 (NAD27). Collection time 1644Z.

Table 2: National Arboretum LiDAR Point Densities. HSI and LiDAR data used for this project. The aircraft altitude was measured in feet above ground level (AGL). The ground sampling distances (GSD) represent the size of a single pixel as it represents the ground from each system.

| Time (Zulu)	Alt. (Feet - AGL)	LiDAR GSD (m)	LiDAR File Name	Minimum Point Density per m²	Maximum Point Density per m²	Mean Point Density per m²
1616	2500	1	Sensor1strip030.las	0.09	12.72	7.61
1628	2500	1	Sensor1strip032.las	0.06	13.14	6.67
1644	2500	1	Sensor1strip035.las	0.00	15.21	7.45
1659	2500	1	Sensor1strip038.las	0.13	16.01	10.51
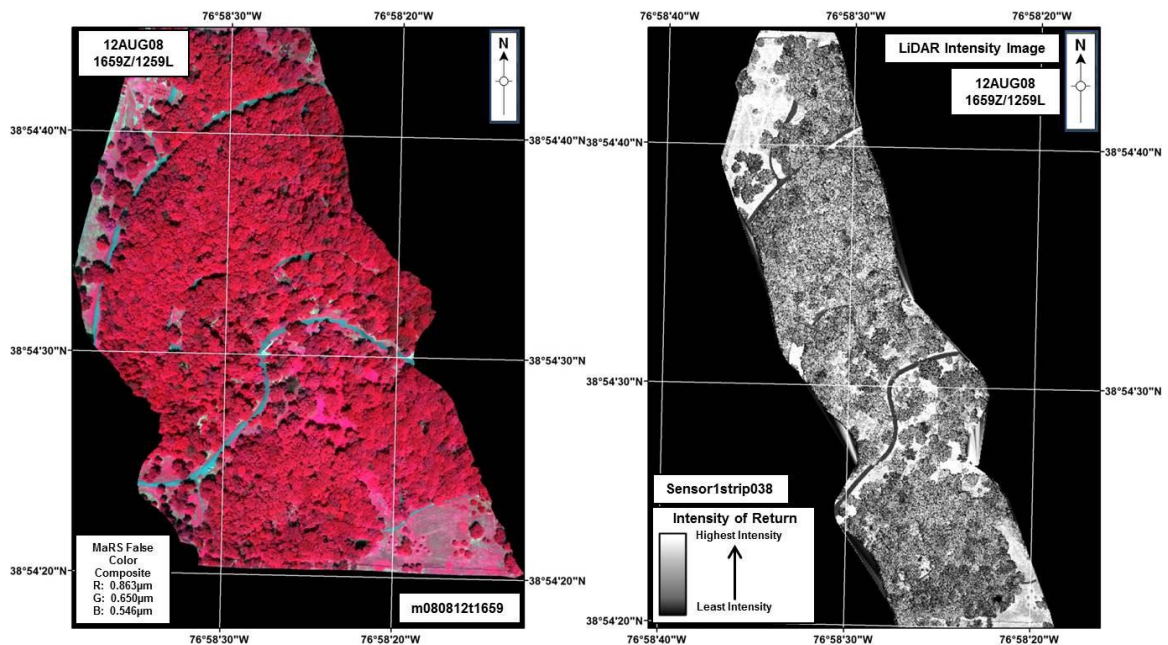
Figure 4: MaRS NIR Composite (left) and Optech ALTM 3100 LiDAR Intensity Image (right) of the National Arboretum, Washington, DC. In the MaRS NIR composite, the red band is displayed as 0.863 μm, green 0.650 μm, and blue 0.546 μm. Both data files have been projected to UTM Zone 18 North, and the datum used is the North American Datum 1927 (NAD27). Collection time 1659Z.

Study Site

The National Arboretum is located in northeast Washington, DC. According to historical flight logs, and also Salvador and Resmini, weather conditions on the day of collection were typical for a DC summer day with temperatures in the mid to upper 80's (°F), but with somewhat low humidity for the area [38]. Unfortunately, limited ground truth was collected during the actual day of collection, which impacts the trails portion of this exercise in particular because the actual conditions of the trails at the time of collection are unknown. Handheld photographs were captured of the American sweetgum trees and also the trails almost exactly 4 years later on Friday, August 3rd 2012. Figure 5

shows a map with several photos of American sweetgum trees that were detected during

this exercise.

Figure 5: Ground truth map showing the capture location of handheld photos of several American sweetgum trees that were mapped during this exercise. Many species on the National Arboretum have tags attached to identify the exact species. One of these tags is visible in Inset 1.

Figure 6 shows a map that includes some pictures of the trails that were mapped during this exercise. Unfortunately, due to the time lapse between airborne data collection and the collection time of these photos, it is not possible to know the exact condition of the trails at the time of airborne data collection. It does seem, however, that the trails may not have been in quite as good of condition during the time of airborne data collection. It appears that when the ground photos were collected, the trails are flusher with a bit more healthy vegetation. It is evident from the MaRS true color and false color imagery that the trails show signs of stressed vegetation, and this can be observed in the full VNIR/SWIR spectrum as well. At the time of handheld photo collation, it may be assumed that inset 2 in Figure 6 is more indicative of the type of condition the trails were in at the time of airborne data collection in 2008. On the contrary, vegetation and trail condition appears much healthier in inset 3 than it does in MaRS imagery from 2008.
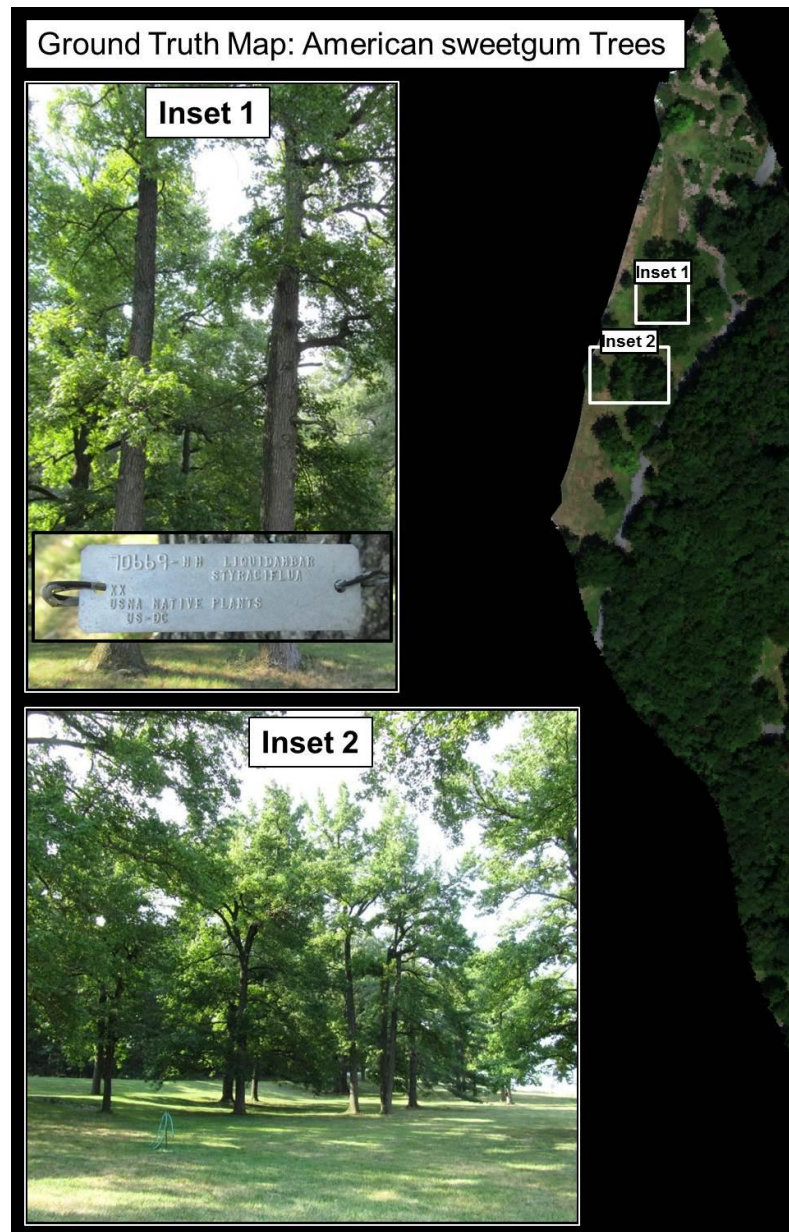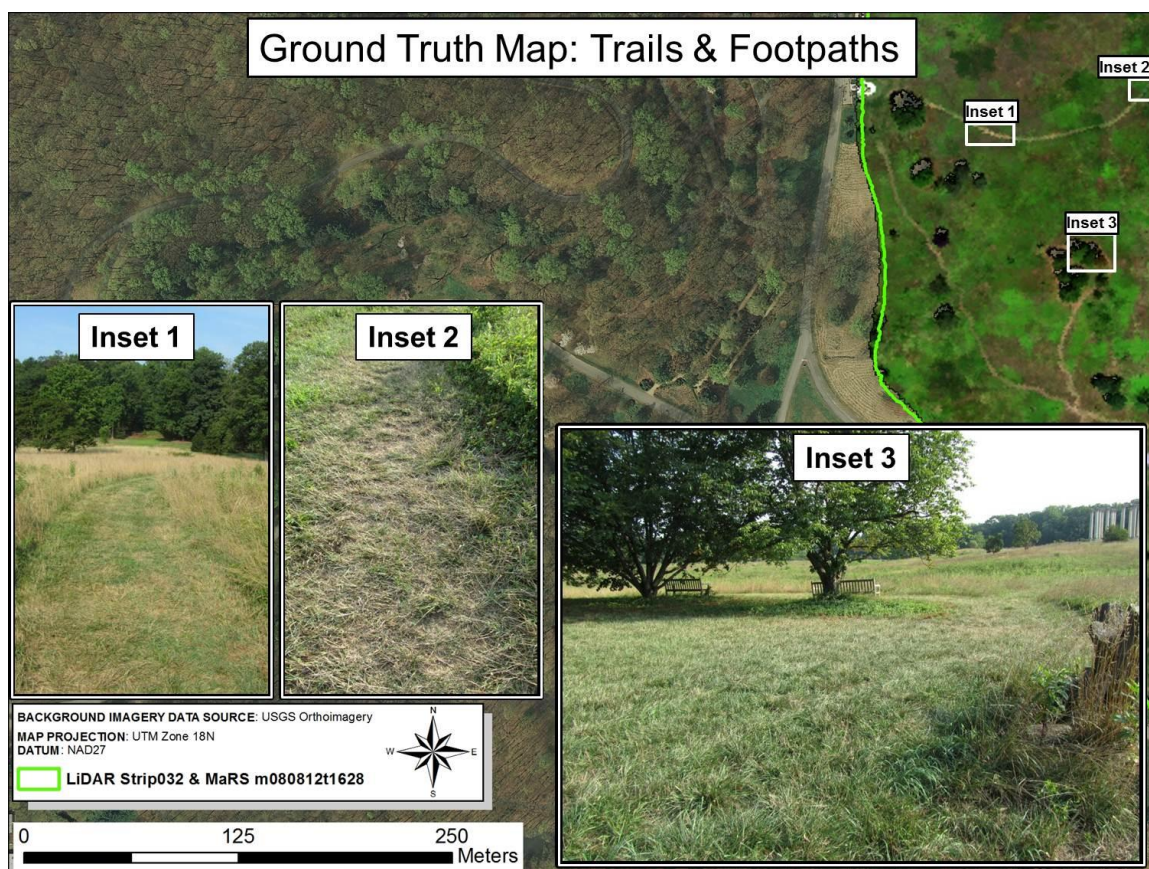
Figure 6: Ground truth map showing the capture location of handheld photos of a few trails and footpaths that were mapped during this exercise. The green line displayed in the figure indicates the swath width of the fused HSI and LiDAR dataset; only a portion of the dataset is shown in the graphic for ease of viewing the inset areas. Trail conditions have probably changed between the time of airborne data collection in 2008 and ground photo collection in 2012.

METHODS

Each step will be explained in detail while all of the steps are outlined in a flow chart. Due to the nature of this HSI and LiDAR fusion project, processing of HSI and LiDAR data occurred almost simultaneously as opposed to, for example, processing all of the HSI data, and then all of the LiDAR data.

Initial LiDAR Processing

In order to initiate the entire process, the first data analyzed was the LiDAR data. The reason for this was because the swath width of the LiDAR data was less than that of the MaRS HSI data. Therefore, it made sense to first preprocess the LiDAR data so that the MaRS HSI data could be spatially subsetted, and thus clipped, to the LiDAR data. Some extremely capable freeware tools provided by the Boise Center for Aerospace Laboratory (BCAL) were used in the initial LiDAR data processing and will be referenced throughout this thesis. These BCAL ENVI® plugin tools [7] are extensively used in this work. The BCAL LiDAR tools are used as an ENVI® plugin while the E3De™ [18] software is used for other processes that are not included in the BCAL LiDAR tools.

Using the subset LAS file(s) function, "Subset via Image/ROI," in the BCAL LiDAR tools [7], the four LiDAR LAS files were manually subsetted to only the National Arboretum study area. New LAS files of the National Arboretum study area were

generated. Next was to determine the overall average point densities of each of the four

LiDAR LAS files. This was achieved using the "Generate Density Map" function in the

E3De™ software; this functionality becomes available to the user once a LiDAR project

is created and LAS files are entered into E3De™. E3De™ outputs the density maps as

TIFF files where the data value within each pixel of each TIFF file represents the overall

point density relative to its geographic area. These images, however, were not sufficient,

by themselves, to determine the necessary statistical point density information. As a

result, each point density TIFF image was individually opened in the ENVI® software.

Statistics were calculated in ENVI® on each point density image to determine the relative

LiDAR point densities of each subsetted LAS file. These point density statistics are

shown in Table 2. Higher point densities are optimal for studying some aspects of

vegetation using LiDAR such as surface roughness, structure, and shape [49] [14].

Moreover, higher point densities should be able to improve classification because,

according to Geerling et al. (2007) [20], such densities should result in better

discrimination between height classes. Dalponte et al. (2009) [14] also used an Optech

ALTM 3100 LiDAR system and achieved point densities of approximately 5.6 points/m^2,

which is slightly lower than the data presented herein. Koetz et al. (2008) [27] was also

using an Optech ALTM 3100 LiDAR system, but it should be noted that the system was

only scanning at a frequency of 70 kHz, and as a result, the LiDAR data presented by

them only has a point density of 3.7 points/m^2. Additionally, Li et al. (2012) [30] report a

LiDAR point density between 6 points/m^2 and 20 points/m^2, and they state that high point

densities such as these are needed to capture the 3D structures of trees. Li et al. (2012)

[30] go on to state that misclassifications can occur where point densities fall short of requirements. In any case, these authors make it clear that higher point densities can result in more accurate LiDAR classifications and thus the average point densities of between 6.6 points/m^2 and 10.5 points/m^2 used for this work are more than optimal for what was achieved here.

The last step that will be briefly discussed in this section is the generation of LiDAR intensity images. LiDAR intensity images provide panchromatic-like context images of each subsetted LAS file in the form of a raster that can be used for subsetting and coregistration of HSI images. The intensity images were generated using the "Convert LAS Data" function in ENVI$^{®}$. The X and Y pixel sizes were set to 1 meter, which was the stated GSD of the Optech ALTM 3100 LiDAR system at the time of collection. With respect to geographic information, the native projection of UTM Zone 18 North was retained, but the datum was converted from WGS84 to NAD27. The NAD27 datum is native to the MaRS HSI data. Keeping the native datum with the MaRS HSI minimized processing time, and also reduced the overall amount of pixel warping that would be caused by switching datums.

Intermediate HSI and LiDAR Processing

An important item to note here that could be somewhat controversial to some is that it was decided to first georegister the MaRS HSI data prior to executing any standard HSI processing steps. One reason for this was that the idea was to process only the HSI data contained within the footprint of the LiDAR data. The only way to achieve this effect was to first apply a georegistration to the MaRS HSI data. Using only the HSI data

contained within the footprint of the LiDAR data provides for a kind of simulation so that, if in the future, HSI and LiDAR fusion were to be taking place in real-time onboard an aircraft similar to Asner et al. (2007) [5], the thought would be to retain only the relevant overlapping data between the two systems. Doing so could possibly save an immense amount of storage space, especially since HSI data files are much larger than the LiDAR. For the purposes of this thesis, if the HSI data were to be processed prior to subsetting to the footprint of the LiDAR data, statistics within the HSI data- but also from outside of the footprint of the LiDAR data- would be used for feature and target detection. Second, direct pixel-based fusion such as incorporating a LiDAR intensity image as an additional band, between the HSI and LiDAR data may not be possible without georegistering the MaRS HSI data prior to traditional HSI processing [35][20]. Geerling et al. not only georegistered their data prior to running filters (in their case, a Maximum Likelihood filter), but also mosaicked the files together so that their entire study area could be processed all at once [20].

Full native georegistration was applied to the four MaRS cubes using Input Geometry (IGM) files provided with the MaRS data delivery. The application of the IGM files to the unregistered MaRS data was accomplished using the "Georeference from IGM" function found in the ENVI® software. It should be noted that elevation is incorporated into the MaRS georegistration process in the form of Digital Terrain Elevation Data (DTED) Level 2. Actual GSD of the MaRS HSI data was computed automatically in ENVI® during this step. These GSD numbers are reported in Table 1.

While the GSD of the MaRS HSI data was slightly better than that of the LiDAR data, it was important to match the GSD of the MaRS HSI data as closely as possible to the LiDAR data. This was accomplished by interpolating (or up sampling) the GSD of the MaRS HSI data to 1 meter. This interpolation was performed in ENVI® using the "Resize Data (Spatial/Spectral)" function. Under this function, there is an option that reads, "Set Output Dims by Pixel Size." Using this option, it was possible to automatically force the MaRS GSD values printed in Table 1 from their original values up to 1 meter by interpolation.

Although the next step of generating LiDAR boundary files could have easily occurred earlier in the process, it was not needed until later, and thus, simply occurred later in the process. The LiDAR boundary files will be used later to subset the MaRS HSI files to match the LiDAR files as closely as possible; this step would not be possible without first having georegistered the MaRS data files. A simple function exists within the BCAL LiDAR tools [7], "Create Boundary EVF/SHP/KML," which allowed for the fast and easy creation of the four LiDAR boundary files in the form of polygons. One important item to note here is that the LiDAR boundary files not only encompass the outer boundary of the LiDAR flight lines, but they also take into account dropped returns. For example, dropped returns could exist over large bodies of water (eg. rivers). Water absorbs most energy at the wavelength of 1.064μm, and can thus result in some dropped LiDAR returns. The polygons obtained from the BCAL LiDAR tools do not include these dropped returns, and thus, areas of dropped LiDAR returns will be removed from the MaRS HSI data during subsetting in the next step.

The last step that will be discussed in this section is the subsetting of the MaRS data to match- as closely as possible at this phase- the footprint of the LiDAR data. This was accomplished by using the "Subset Data by ROI" function in the ENVI® software. Prior to running this function, the four LiDAR boundary files were loaded into ENVI® as vector files while the four corresponding georegistered MaRS HSI cubes were loaded as well. While running the function, it was imperative that the proper LiDAR boundary file was chosen to correspond with the correct MaRS HSI cube. For example, according to Table 1, MaRS cube "m080812t1616" needed to be subsetted using the boundary file from the LiDAR LAS file "Sensor1strip030;" these two datasets were collected coincidentally. Moreover, a key item to note is that there is a switch that asks if users want to "Mask pixels outside of ROI." For this type of data fusion, the switch should be set to "yes." This switch eliminates any MaRS HSI data outside of the LiDAR footprint by excluding MaRS data outside of the LiDAR boundary file. It should be reiterated that this step could not have taken place if the MaRS HSI data were not already georegistered. Figure 7 shows an example of one of the coincidentally collected MaRS HSI and LiDAR data pairs almost exactly coregistered where the footprint of the MaRS HSI data has been closely matched to that of the LiDAR data. A more precise coregistration using tie points will follow.
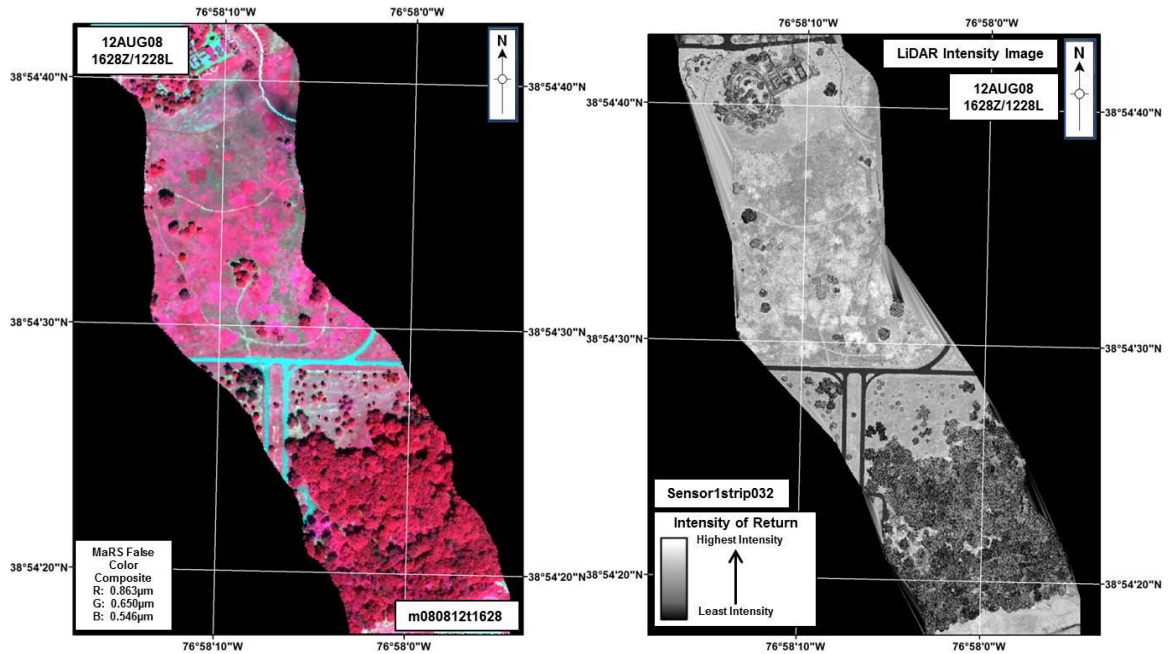
Figure 7: MaRS HSI data (left) subsetted to Optech ALTM 3100 LiDAR data (right). Tie point registration in subsequent steps will provide a more exact registration between the two data types.

Traditional HSI Processing

This section will discuss traditional HSI data processing that was performed on the MaRS data prior to executing any filters or detection algorithms. Spectrally, there is a focal plane overlap region in that MaRS data that corresponds to band numbers 112 – 121 [42]. These bands are automatically delivered as zero value bands, and are the first to be removed (subsetted). The "Resize Data (Spatial/Spectral)" function in ENVI® was used to remove these bands. Subsequent to removing these overlap region bands, each data cube contained 322 spectral bands. Spatially, there is a physical gap between the VNIR and SWIR focal planes that results in an offset of 40 pixels. Prior to data delivery, MaRS calibration software automatically corrects for this offset by shifting the VNIR and SWIR data into place so that they are properly aligned. This shifting results in 15 zero value lines (columns) on the left side of the data cubes and 25 zero value lines (columns) on the

right side of the data cubes. These zero value lines are thus removed from each data cube, which results in data cubes that are 600 lines across. The "Resize Data (Spatial/Spectral)" function in ENVI® was used to remove these lines.

Atmospheric correction was the next step. In order to make the HSI data useable for the purposes of material detection, it must be converted to reflectance [44]. Reflectance data are needed so that the in-scene spectral absorbance material features are more evident and can then easily be compared to a library of known reflectance spectra. The MaRS HSI data were delivered in calibrated radiance in the following units:

$$\frac{W}{M^2} SR^{-1} \mu m^{-1}$$

The Quick Atmospheric Correction (QUAC) method was used to convert the four MaRS HSI data cubes from units of radiance to unit of reflectance [8]. In an effort to save storage space, the calibrated data are delivered in two-byte signed integer format. As a result, when converted to reflectance using QUAC, data are scaled between 0 and 10,000 where "0" is considered 0% reflectance and 10,000 is considered 100% reflectance.

Once the atmospheric correction was performed, routine atmospheric bad band removal (spectral subsetting) was achieved. Bad band removal was completed manually in several iterations using the ENVI® software with the "Resize Data (Spatial/Spectral)" function. The first iteration involved opening the MaRS HSI data cubes in ENVI® and animating the spectral bands. Spectral bands that contained unreasonable amounts of noise were removed. The second iteration involved opening each of the data cubes and examining known areas of in-scene reflectance spectra such as water, vegetation, and soil for spectral discrepancies. Often, additional subtle discrepancies not discovered during

spectral band animation can be noted around water vapor absorption features' border areas along the wavelength dimension where the atmosphere does not transmit electromagnetic radiation. Many of these areas are due to water vapor; however some of them could also be due to sensor noise or outside interference. A complete list of bands removed along with the reasoning is provided in Table 3. For consistency, the same bands were removed from each MaRS HSI data cube.

Table 3: Bad Bands Removed

Spectral Band Numbers Removed	Corresponding Wavelengths (µm)	Reason for Removal
1 – 12	0.386 – 0.430	Too little signal provided by the system in this region results in unreasonable noise
112 – 121	0.829 – 0.853; 0.806 – 0.822	Focal Plane Overlap Region
135 – 136	0.935 – 0.943	H_2O inhibits atmospheric transmission in this region
158 – 161	1.120 – 1.144	H_2O inhibits atmospheric transmission in this region
185 – 200	1.337 – 1.457	H_2O inhibits atmospheric transmission in this region
241 – 268	1.787 – 2.004	H_2O inhibits atmospheric transmission in this region
323 – 332	2.446 – 2.518	Some H_2O and CO_2, and little signal provided by the system in this region results in unreasonable noise

The last step of HSI processing that could be considered a form of traditional preprocessing, but was specific to this thesis topic, was to separate the MaRS HSI data into VNIR, SWIR, and VNIR/SWIR datasets, respectively. Splitting the MaRS HSI data into these three categories allows for individual testing and scrutiny of each spectral region during the HSI and LiDAR fusion process, which is the goal of this thesis. The MaRS HSI data were split into these three spectral regions in ENVI® using the "Resize

Data (Spatial/Spectral)" function. A total of twelve MaRS HSI data cubes were generated

as a result of this splitting (four original VNIR/SWIR, four VNIR-only, and four SWIR-

only). Table 4 provides the specifics of the three spectral regions chosen for analysis.

Table 4: Split MaRS HSI Spectral Regions

Spectral Region	Number of Bands Contained within Image Cube	Corresponding Wavelengths (μm)
VNIR-only	125	0.434 – 1.040
SWIR-only	125	1.050 – 2.430
VNIR/SWIR	250	0.434 – 2.430

It is only coincidental that the "VNIR-only" and "SWIR-only" spectral regions listed in

Table 4 contain the same number of bands. Additionally, extending the VNIR region out

to 1.04μm could be considered one source of contention, but it should be noted that some

VNIR-only spectral systems such as WorldView-2 extend out to 1.04μm [6].

Tie Point Coregistration of HSI and LiDAR

In order to achieve the accuracy necessary for this type of data fusion work, the

coregistration between the MaRS HSI and LiDAR data files not only had to be accurate,

but it also had to be precise. Although the HSI and LiDAR data were collected

coincidentally onboard the same aircraft, the two systems exhibit slightly different

behavior with respect to the accuracy of their native georegistration. Naturally, the MaRS

HSI system is less accurate than the LiDAR geospatially for a few reasons, one of which

can be attributed to distortions in the optical lens that can be difficult to correct even with

some of the most accurate modeling. If such registration inaccuracies are not corrected,

visibly noticeable offsets will exist between the two datasets that would probably result in

classification errors. For example, due to registration inaccuracies a road could exist in the HSI data at the same place where a building lies in the LiDAR data, which would result in erroneous classification results.

So that such errors are prevented, a combination of custom semi-automated tie point coregistration methods was executed using the ENVI® software. Each of the four flight lines that consisted of one HSI data file and one LiDAR data file had to be coregistered. Since the native LiDAR georegistration was already highly accurate, the MaRS HSI data files were warped to the LiDAR files. The previously generated LiDAR intensity images at 1.064 μm were used as the base images during the coregistration process. Likewise, Mundt et al. (2006) [31] stated that it would be advantageous to use the reflectance band in the HSI that most closely matched the wavelength of the LiDAR intensity image. There exists a MaRS spectral band at 1.06392 μm, and this was the MaRS band chosen for the coregistration process. Approximately 20 seed points were first selected for each combination of images using the "Select GCPs: Image to Image" functionality in ENVI®. Next, the seed points generated in ENVI® were imported into the ENVI® "Image Registration Workflow" tool (only available in v5.0). The matching method used to automatically generate more tie points based on the manually generated seed points, was the "[Cross-Modality] Mutual Information" method with the setting "Minimum Matching Score" of 0.005. The "Geometric Model" used was "Fitting Global Transform" with a "Transform" of first-order polynomial. For each data file, the total number of tie points generated and the average root mean squared RMS error is listed in Table 5.

Table 5: HSI and LiDAR Coregistration Information

HSI File Name	LiDAR Intensity File	Total Number of Tie Points Selected	Mean RMS Error
m080812t1616	Sensor1strip030	78	0.72
m080812t1628	Sensor1strip032	108	0.61
m080812t1644	Sensor1strip035	155	0.60
m080812t1659	Sensor1strip038	77	0.59

It should be noted that the first file set, HSI file m080812t1616 and Sensor1stip030, exhibited a mean RMS error that is much larger than the other three values. This deviation is due to there being far fewer discernible features between the two datasets; much of this flight line contained a forested area.

Once each of the sets of tie points was generated and considered acceptable, the full VNIR/SWIR MaRS cubes were the first to be warped. The tie points were saved and applied to the remaining VNIR-only and SWIR-only HSI files were coregistered using the same four sets of tie points. This operation was completed using the "Select GCPs: Image-to-Image" function in ENVI®.

Figure 8 and Figure 9 are LiDAR images that have been color sharpened using the coincidentally collected MaRS HSI images; this is also the first illustrated example of pixel-level fusion given in this document. The method of color sharpening chosen was hue, saturation, and value (HSV), and was performed using the "Image Sharpening" function in ENVI®. The reader may note some vivid color spots in the images. Most of these are due to shadowing in the MaRS HSI images that is not present in the LiDAR imagery. Extremely low (dark) values contained in the areas of these shadows in the

MaRS HSI images cause the HSV algorithm to exhibit slightly erroneous results due to the low dynamic range in these areas, which can be expected. The true color VNIR MaRS bands chosen for color sharpening corresponded to the wavelengths at 0.638 µm (red), 0.550 µm (green), and 0.458 µm (blue). Additionally, the HSV color sharpened LiDAR images presented in Figure 8 and Figure 9 also visually demonstrates the overall accuracy, precision, and proficiency of the tie point coregistration performed between the MaRS HSI and LiDAR datasets.

Specialized LiDAR Processing

This section will cover the processing of LiDAR data unique to this topic of HSI and LiDAR fusion for vegetation and background discrimination. There does not yet seem to be a standard set of procedures for this type of data fusion processing; rather, the previous studies cited thus far have each performed the HSI and LiDAR fusion somewhat differently. As a result, the LiDAR processing presented herein will include some combinations of methods that have been executed by previous authors.

Prior to generating vegetation raster products using the BCAL LiDAR tools, the LiDAR data had to be processed into ground and vegetation classes. This processing technique was used to automatically determine which LiDAR points are ground returns, which LiDAR points are vegetation returns, and of the vegetation returns, the height of those returns above the ground. This processing technique, "Perform Height Filtering," is found in the BCAL LiDAR tools, and is attributed to Streutker and Glenn (2006) [43]. Operating the tool was rather straightforward; the subsetted LAS files are selected and only a few parameters were set; canopy spacing was set to 4 m, and the maximum

allowable height was set to 40 m to eliminate outlying LiDAR returns. New height

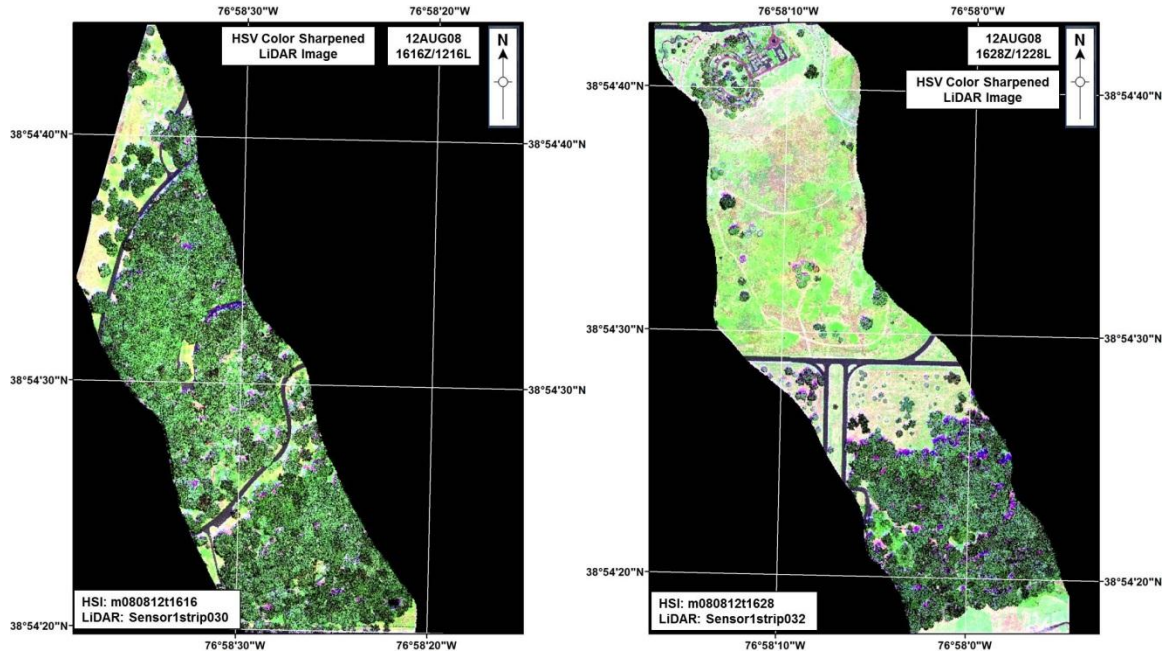filtered LAS files were generated and saved in the designated output directory.

Figure 8: HSV color sharpened LiDAR images. Zulu time 1616 (left) and Zulu time 1628 (right). The corresponding MaRS wavelengths used for the color sharpening are 0.638 µm (red), 0.550 µm (green), and 0.458 µm (blue). Spotty exuberant discolorations are caused primarily by shadows in the HSI images that are not present in the LiDAR images.
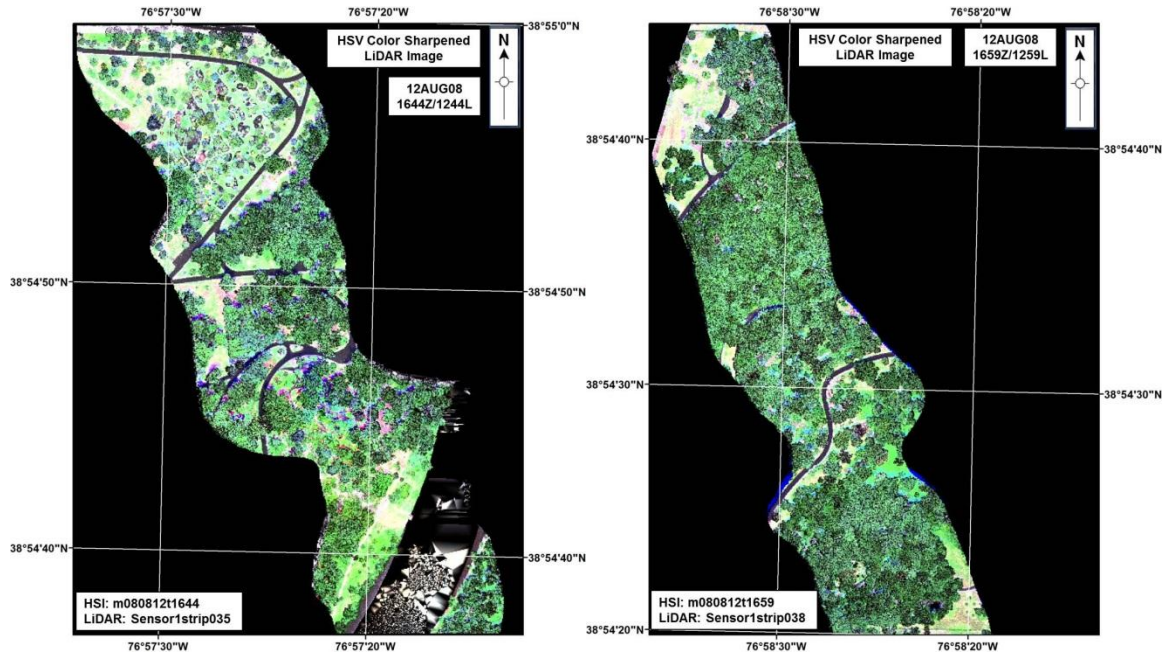
Figure 9: HSV color sharpened LiDAR images. UTC time 1644 (left) and UTC time 1659 (right). The corresponding MaRS wavelengths used for the color sharpening are 0.638 µm (red), 0.550 µm (green), and 0.458 µm (blue). Spotty exuberant discolorations are caused primarily by shadows in the HSI images that are not present in the LiDAR images. Some edge effects may also be observed.

Once the height filtered LAS files were generated, specific raster transformations could be produced from the LiDAR data using the BCAL LiDAR tools. Many options were explored with respect to which transformations would work best for this type of analysis. Asner et al. (2008) [4] used the LiDAR data in order to compute vegetation height, crown shape, and a DSM. These transformations were immediately fused with the HSI data to generate additional filters that would not have been made possible without the LiDAR data. Dalponte et al. (2009) [14] chose to use only the elevation and intensity of the LiDAR data. Onojeghuo and Blackburn chose to use the CHM, DSM, and slope, but it should be noted that these were used as masks for the HSI data, and thus, this represents feature-level fusion as opposed to pixel level [32]. Geerling et al. (2007) [20]

chose to compute the minimum, maximum, mean, median, standard deviation, and range of height as transformations.

Similarly, for this project, the following LiDAR transformations were chosen for vegetation analysis:

- Vegetation Roughness

  - The vegetation roughness is calculated as the standard deviation of all the height point returns within each raster pixel. [7] [17]

- Vegetation Height: Minimum

  - The minimum vegetation height is calculated using the minimum vegetation height point return within each raster pixel. [7] [17]

- Vegetation Height: Maximum

  - The maximum vegetation height is calculated using the maximum vegetation height point return within each raster pixel [7] [17].

- Vegetation Height: Range

  - The vegetation height range is calculated by subtracting the maximum vegetation height point return from the minimum vegetation height point return within each raster pixel [7] [17].

- Vegetation Height: Mean

  - The mean vegetation height is calculated by taking an average of the height of the point return within each raster pixel [7] [17].

- Vegetation Height: Variance

- The vegetation height variance is calculated using the statistical variance of all height point returns within each raster pixel [7] [17].

- Number of LiDAR Vegetation Returns
  - The number of LiDAR vegetation returns is the sum of all point returns within each pixel that were classified as vegetation. [7] [17]

- Vegetation Cover
  - The vegetation cover is calculated by dividing the sum of all point returns within each pixel that were classified as vegetation by the total number of LiDAR returns contained within each pixel. [7] [17]

Each of the above LiDAR raster transformations can be fused with the MaRS HSI data as an additional band. This should be extremely useful in reducing the number of false alarms that will come out of traditional HSI processing such as Mahalanobis Distance or SAM filtering. For example, if a pixel rings positive for vegetation using a SAM filter in the HSI, that same pixel in the vegetation cover LiDAR transformation may have no results (i.e., a value of zero) for vegetation, which would negate this pixel as a positive detection. Likewise, with regards to vegetation species delineation and mapping, a training pixel could have a perfect HSI vegetation signature with a strong red edge, but will also have a maximum height value associated with it from the LiDAR data. Although many types of vegetation may present similar spectral signatures, the height values could vary by orders of magnitude, and as a result, this height value will continue to help to reduce the number of false alarms in the final filtering phase. Note that a LiDAR intensity image is not included as one of the above LiDAR transformations. Since

the MaRS HSI data collected includes a band that is practically at 1.064μm, it did not

seem necessary to include the LiDAR intensity image, which would be including

redundant information. On the contrary, if this work utilized an HSI system that did not

include a band at or near 1.064 μm, then it would be appropriate to include the LiDAR

intensity image as part of the project.

Figure 10 shows an example of a fused MaRS HSI and LiDAR image where the

true color values corresponding to green and blue are used in conjunction with the

LiDAR vegetation roughness transformation. Generally, red areas are vegetated.

However, brighter red areas correspond to regions of greater vegetation roughness.

Figure 10 shows similar results to those previously published by Geerling et al. (2007)

[20].

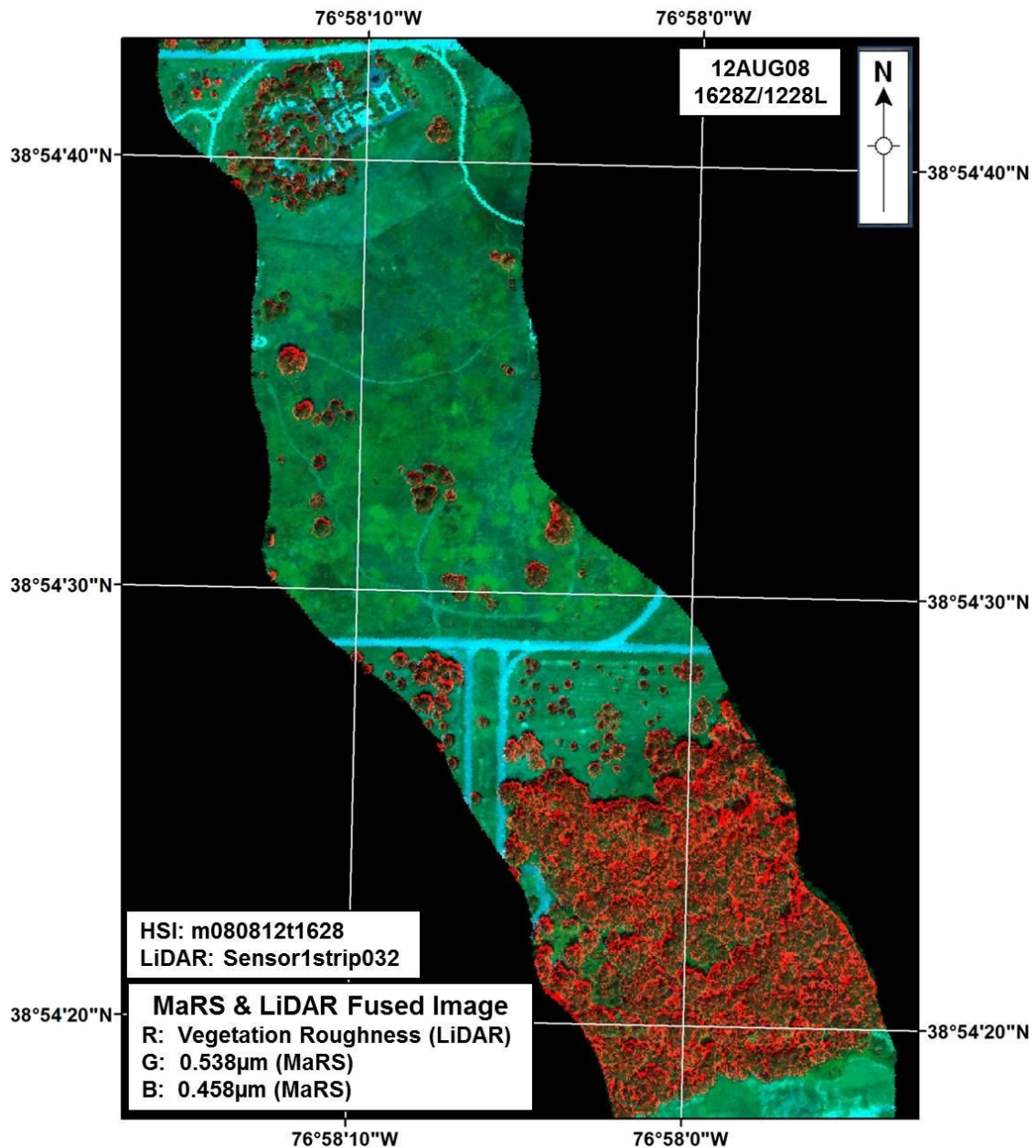**Figure 10: A fused MaRS HSI and LiDAR image; regions of brighter red correspond to higher vegetation roughness values as a result of LiDAR processing. Similar to results in Geerling et al. [20].**

Additional LiDAR Transformations for Trails Analysis

In addition to the eight transformations listed above, there were five additional

LiDAR transformations that were added in to the layer-stacked file specifically for the

purposes of finding trails and footpaths. Since it is assumed that trails and footpaths are

essentially bare earth, the five additional LiDAR transformations were calculated using

bare earth parameters. Although vegetation transformations can be useful layers for the

purposes of finding trails, these layers will not be used to locate vegetation here; rather,

they will be used to find where there is no vegetation. In other words, when searching for

trails, a value of 0 or close to 0 should be expected at the location of a trail in layers such

as vegetation roughness, number of LiDAR vegetation returns, and vegetation cover.

Since most of these layers may contain values closer to 0 where a trail exists, the addition

of the following layers was deemed necessary:

- Bare Earth Absolute Roughness
    - The bare earth absolute roughness is calculated as the standard deviation
      of all points within each pixel classified as bare earth elevation. Note: The
      bare earth elevation is calculated by subtracting the vegetation height from
      the data elevation [7].
- Bare Earth Local Roughness
    - The bare earth local roughness is calculated just as the absolute roughness,
      however, the local slope has been removed first [7].
- Bare Earth Slope (degrees)
    - The bare earth slope is calculated using the mean of all points classified as
      bare earth within each pixel [7].
- Bare Earth Aspect (degrees from N)

o The bare earth aspect is calculated by finding the aspect of the average

slope of all points classified as bare earth within each pixel [7].

- Ground Point Density

  o The ground point density is calculated by finding the density of all points

  classified as bare earth within each pixel [7].

Although this hypothesis will go untested, the use of these five additional transformations for the purposes of locating trails should yield better results than if the vegetation transformations were used alone. These additional transformations will be stacked on top of the eight vegetation transformations mentioned above to form a 13-band, stacked LiDAR transformation image cube.

LiDAR Transformation Stacking

The eight LiDAR transformations listed above (and for trails analysis, the five additional bare earth transformations) are stacked into a single image and normalized so that they could be fused with the MaRS HSI data. Some of the transformations contained values between 0 and 1 while other transformations would contain values between 0 and 100 or more. Hence, all of the transformations had to be normalized, or scaled to between 0 and 1, to be equivalent to the scale of the HSI data. The transformations were first stacked into a single image cube in ENVI® using the "Layer Stacking" function. Next, an equation and a code program provided by Dr. Ronald Resmini were used to scale the transformation between 0 and 1.

$$\frac{\rho - \rho_{min}}{\rho_{max} - \rho_{min}}$$

Equation 1: Data normalization

This equation would result in small subsets of negative values in each of the

transformations, especially near edge pixels with already low values. These negative

values had to be removed so that the scale would remain aligned with the HSI data. These

values were easily set to 0 by using the "Band Math" function in ENVI®, and setting the

stacked and normalized transformation image cube file greater than 0 using "B1>0." The

scale, however, was still not finalized. Since the HSI data files started in an integer

format, the reflectance values were scaled between 0 and 10,000 instead of 0 to 1. As a

result, the stacked and normalized LiDAR transformation file simply had to be multiplied

by 10,000 so that the LiDAR transformation values would read between 0 and 10,000 as

opposed to 0 and 1.

Locating Exploitable Tree Species on the National Arboretum Study Site

Although it may seem that there are many trees and tree species at the National

Arboretum, locating ones to satisfy the needs of this study was challenging. Many of the

plant species at the National Arboretum only occur in pairs, and for this study, it was

necessary to have more than one or two of a single species for testing and evaluation

purposes. It would be rather easy to map a pair of trees if these were the only two trees

used in the training sample during raster processing. An AutoCAD® file containing

ground truth information on the National Arboretum (as of 2008) was obtained from the

National Arboretum. This file type can be imported into ArcGIS®, but it was found that

there was no geolocation information associated with it. As a result, the AutoCAD® file had to be manually warped and georeferenced to overlay properly onto the MaRS and LiDAR data. The projection and coordinate system of NAD27, UTM Zone 18N, was also matched to the data. The flow chart for this GIS process is shown in Figure 11.

Once imported into ArcGIS®, it was found that the AutoCAD® file contained five separate layers: points, lines, polygons, multipatch, and annotation. The point and polygon layers were exported as shapefiles and would be used for geolocation and subsequent processing. The Georeferencing Toolbar in ArcGIS® was used to accurately geolocate the exported shapefiles. The polygon shapefile contained a column called "RefName," which contained an attribute called "Canopy." These "Canopy" polygons represented the canopies of certain tree species at the arboretum. If there were any trees species where multiple plants were represented on the ground with large canopies (i.e. over 100 m^2), such larger canopy species would be easier to locate visually in the MaRS and LiDAR images for ground truth purposes. These canopy polygons were exported as a separate shapefile, and since the shapefiles are georeferenced, the shape area could be calculated. Only 115 of the 6,215 shapes contained the canopy attribute; thus the canopies of only 115 plants had been extracted (mainly the larger plants). Unfortunately, the canopy polygons did not contain the plant names. As a result, the plant names had to be extracted from the point shapefiles. A standard "Select by Location" was executed in ArcGIS® to find which of the canopy shapes intersected the point shapes. It was determined that, of the total canopy shapes that were within the swath widths of the fused HSI and LiDAR data, 16 were determined to be of the same species: *Liquidambar*

styraciflua, or American sweetgum. There were, however, five additional American sweetgum tree shapefile points in the same general area that did not have associated canopy shapefiles, but will most certainly be useful during the ground truth portion of this exercise.

Figure 12 shows a map of the American sweetgum trees and the location of the imagery data files. Some of the Arboretum plants, depicted by polygons, lay outside of the swath width of the project data, and cannot be used for this exercise. Slight differences between the data boundary shapefiles and the two MaRS files shown are due to the boundary shapefiles being generated prior to the tie point registration of the MaRS and LiDAR data. Background publicly available orthoimagery was acquired from the United States Geological Survey (USGS). The true color USGS orthoimagery collected in April 2010 has a 0.16 meter GSD [45].

There were a large number of *Quercus phellos*, or Willow Oak trees, but these were unfortunately outside of the swath width of the project data. Salvador and Resmini were able to make use of the Willow Oak for their study because they did not use the LiDAR data, which would have limited the swath width of their HSI data and thus their use of the Willow Oak for ground truth purposes [38].
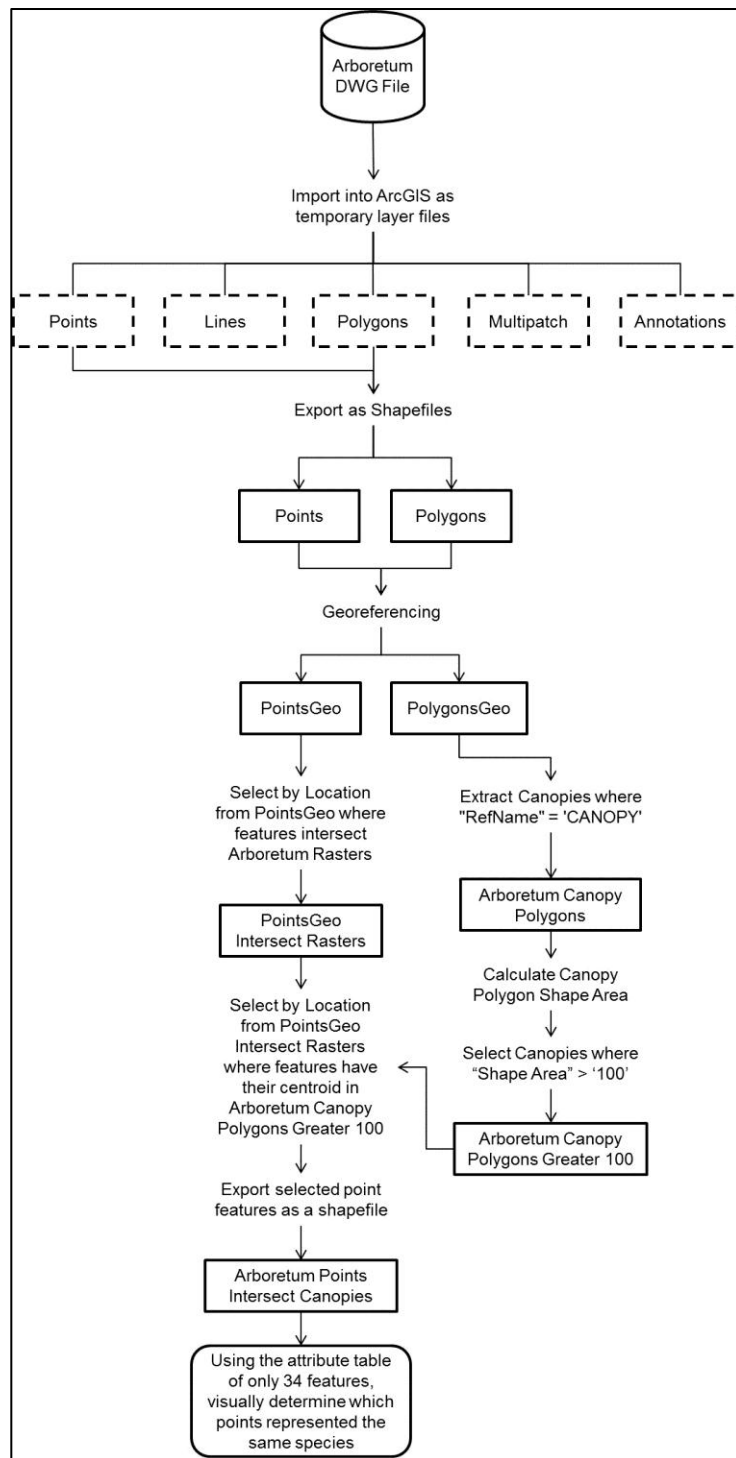
Figure 11: This flow chart shows the steps used to determine that the American sweetgum would be a good ground truth source for this project. The use of a GIS helped to determine which tree species would be good for ground truthing.

50
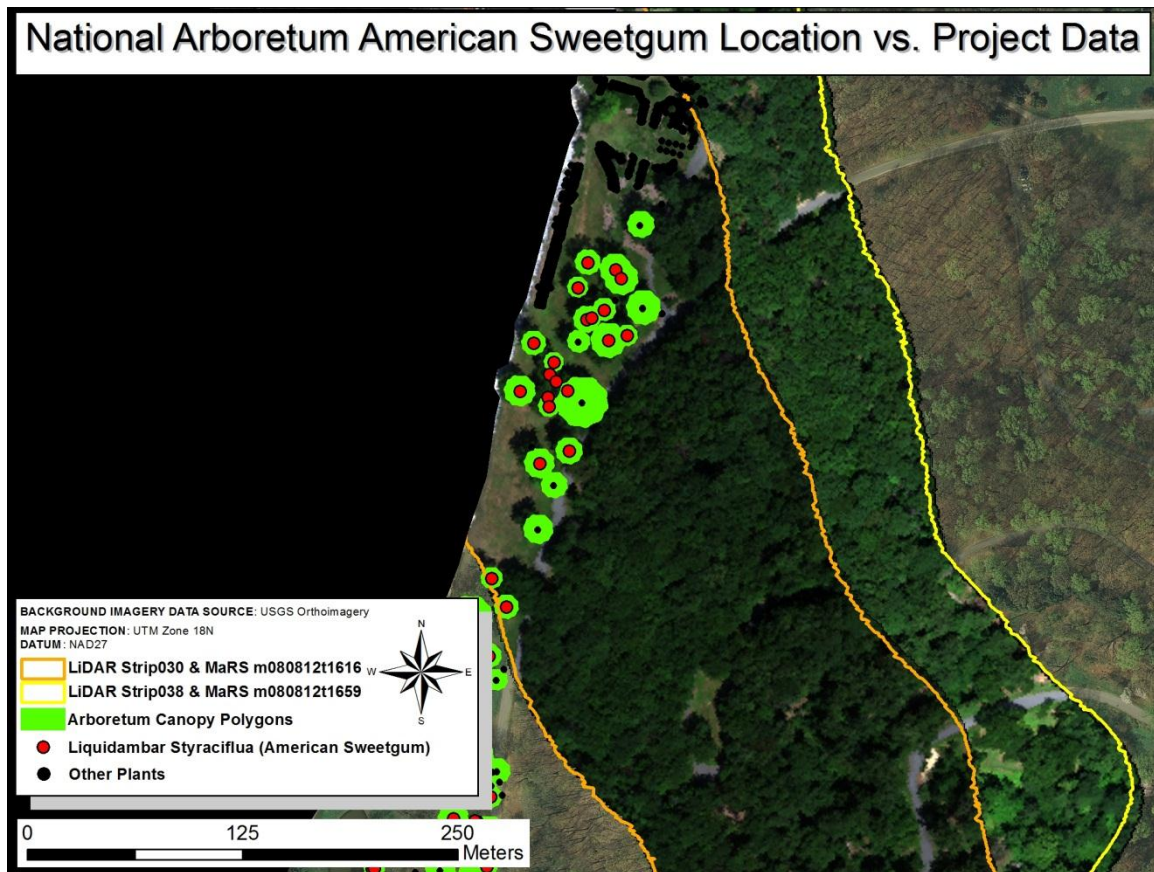
Figure 12: Map of the location of American sweetgum trees vs. project data files. The two MaRS images (shown here subsetted to the LiDAR data) and USGS orthoimagery are displayed as true color composites. Shadows extending out from some of the tree canopies could make the location of the tree canopy polygons deceiving to the viewer.

Locating Trails for Exploitation

In addition to the American sweetgum trees, some trails located within the

National Arboretum study site were chosen for background materials and target analysis.

Locating mappable trails for this type of work was not as straightforward as locating a set

of trees. The National Arboretum AutoCAD® DWG ground truth file that was converted

to shapefiles did not contain information on trails or footpaths. Moreover, although the

District of Columbia Geographic Information System (DC GIS) offers some shapefiles

related to trails in Washington, DC, these shapefiles did not seem to include trail

information for the arboretum. As seen in Figure 13, sidewalk and street information was

included in shapefiles offered by DC GIS. This information was useful because it

provided ground truth to eliminate any confusion related to what might have been an

unpaved trail versus a paved sidewalk or street. A few trails were located in MaRS cube

m080812t1628 coincidentally with LiDAR Strip032. Using the "ROI Tool" in ENVI®,

visible trails were extracted manually as a raster region of interest (ROI). These manually

extracted trails can also be seen in Figure 13. An important note about this analysis is that

these trails represent footpaths that blend in with the natural vegetated background. These

trails most certainly do not represent every type of trail that exists in the environment. For

example, in arid regions, trails could be the result of substantial foot or vehicular traffic

dispersing and overturning rock and sand resulting in other types of exposed minerals

than those visible in the natural background. Trail types are mostly unique to the

environment in which they exist, and although some generic methods can be used to

extract such trails, analytic judgments must be made as to what type of analysis must be

conducted in order to extract them.
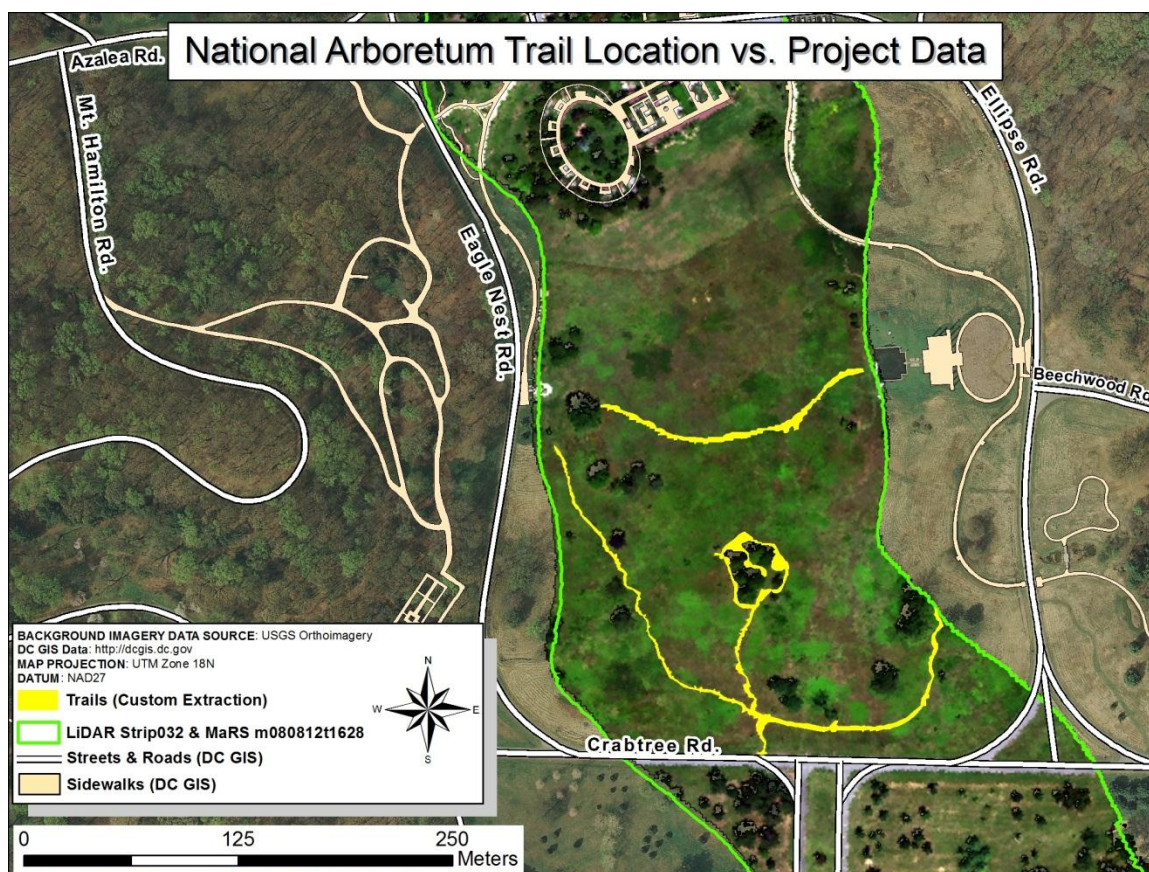
Figure 13: Map of the location of the trails to be analyzed vs. project data. The trails were extracted manually using ArcGIS®. MaRS data cube m080812t1628 is displayed as a true color composite.

Specialized MaRS HSI Data Processing

A total of five in-scene methods were chosen to map the American sweetgum in

MaRS cube m080812t1616. This cube was chosen as opposed to the adjacent cube,

m080812t1659, because it encompassed a larger number of American sweetgum trees. It

can be seen in Figure 1, Figure 4, and Figure 12 that both cubes also have large amounts

of other vegetation species within them, which creates the possibility for false alarms in

the datasets. Nine pixels were chosen from two separate American sweetgum trees as the

training ROIs. Thus, the training ROI was a total of 18 pixels. The mean spectral

reflectance signature of these 18 pixels was used for mapping. The five algorithms

chosen for sweetgum mapping were MF, MTMF, ACE, SAM, and principal component

(PC)-rotated SAM. The PC-rotated SAM was also utilized by Salvador and Resmini

(2009) [38]. There was interest in using other algorithms such as Mahalanobis distance

and maximum likelihood, but these algorithms require a larger training sample. Since

there were already so few American sweetgum trees in the scenes of interest, choosing

large training ROIs for these other algorithms would not be possible. Figure 14 shows the

location of the two training ROIs chosen for the in-scene American sweetgum mapping.

The same ROIs, the same set of LiDAR-derived transformations, and algorithms were

used for each of the VNIR, SWIR, and VNIR/SWIR analysis.

Some of the filters mentioned above need further description. A standard means

of using the MTMF in ENVI® is to first compute the MTMF using the Minimum Noise

Fraction (MNF) [10]. The user then opens a 2D scatter plot with the infeasibility on the

y-axis and the MF score on the x-axis. Pixels with low infeasibility values and high MF

values are target pixels. Since filter planes must be stacked for this exercise, the

scatterplot method was not practical. As a result, when referred to herein, MTMF is the

filter plane that is the result of the MF divided by the infeasibility, which is also scaled

from 0 to 1.

Additionally, the SAM filter planes required further processing. Filter planes

produced by the SAM algorithm produce target pixels with low values. In other words,

values closer to zero in a SAM filter plane are those that indicate a match. Since the filter

planes must be stacked into one image for this exercise, not only must all of them be

scaled from 0 to 1, but the target pixels must also be all high values. Consequently, the SAM filter planes had to be inverted so that the low values became high values. This way, the SAM filter planes would be in line with the MF, MTMF, and ACE filter planes where values closer to 1 are the target pixels. Dr. Ronald Resmini provided a C code program that inverted the SAM filter planes. The PC-rotated SAM worked well for Salvador and Resmini when mapping vegetation in the National Arboretum [38]. A standard Principal Components Analysis (PCA) is first performed, and then SAM is performed on the PCA using the American sweetgum (or trails) training ROIs. These signatures are in PCA space as opposed to reflectance space. The same SAM filter plane inversion must also be applied to the PC-rotated SAM filter plane so that the target pixels have values closer to 1.

Like the sweetgum analysis, nine pixels were chosen from two separate portions of the trails to be mapped as the training ROIs. Thus, the total size of the training ROI was 18 pixels. The same five HSI algorithms were chosen for trail mapping: MF, MTMF, ACE, SAM, and PC-Rotated SAM. There were, however, some additional HSI filters that would be added to the trails analysis in an attempt to make the mapping of such trails simpler. Figure 15 shows the location of the two training ROIs chosen for the in-scene trails mapping.
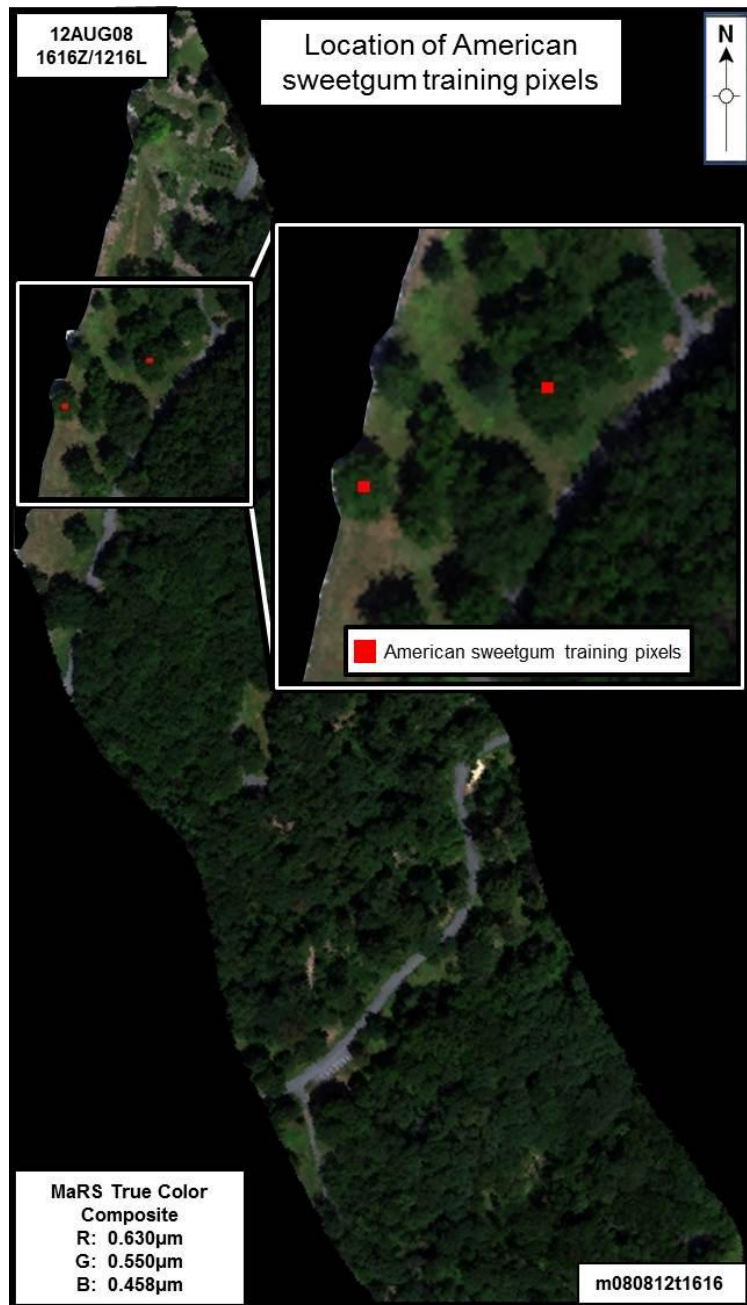
Figure 14: Location of the training pixels selected for American sweetgum analysis.

Figure 15: Location of the training pixels selected for trails analysis.

Additional HSI Filters for Trails Analysis

Similar to the addition of transformations in the LiDAR processing, several HSI-derived filters based on various indices were also chosen to be added to the trails analysis. Not all of the HSI filters could be generated using every part of the spectrum; some of the HSI filters work only in the VNIR, only in the SWIR, and some use bands from both the VNIR and the SWIR. Thus, only the HSI filters corresponding to the appropriate parts of the spectrum were added to each portion of the analysis. For

example, if a filter used only bands from the VNIR, it was added to the VNIR-only

analysis, and was not included in the SWIR-only analysis or the full VNIR/SWIR

analysis. The additional HSI filters chosen were the following:

- Atmospherically Resistant Vegetation Index (ARVI, VNIR-only & VNIR/SWIR)

$$ARVI = \frac{NIR - 2\ RED - BLUE}{NIR + 2\ RED - BLUE}$$

Equation 2: ARVI [26]

  o The ARVI is effectively an enhanced Normalized Difference Vegetation

     Index (NDVI) that is designed to account for atmospheric factors such as

     aerosols [26] [19]. This filter was useful in separating trails from the

     background. Although the reasoning behind the usefulness of ARVI for

     these purposes may not be fully understood, Kaufman and Tanre (1996)

     [26] show that the ARVI value is lower than that of a NDVI value,

     especially in areas where vegetation is not present. As a result, ARVI

     could be providing slightly increased discrimination between background

     areas and fully vegetated areas.

- Simple Ratio Index (VNIR-only & VNIR/SWIR)

$$SR = \frac{NIR}{RED}$$

Equation 3: SR [37]

- o This Simple Ratio Index takes a band of high vegetation chlorophyll

  reflectance from the NIR region of the spectrum, and divides it by a band

  from the red portion of the spectrum. Similar to ARVI, this helps to

  separate trails by indicating areas of healthy and unhealthy vegetation [37]

  [19]. Trails would be associated with stressed vegetation (i.e., unhealthy

  vegetation) due to crushing and trampling associated with trail usage.

- Structure Intensive Pigment Index (SIPI, VNIR-only & VNIR/SWIR)

$$SIPI = \frac{0.800\mu m - 0.445\mu m}{0.800\mu m - 0.680\mu m}$$

Equation 4: SIPI [34]

- o SIPI utilizes bands that are directly linked with vegetation pigments.

  Increases in SIPI values may be linked with increased vegetation canopy

  stress. SIPI may be used to detect physiological stress in plants. Thus,

  SIPI shows good results with respect to trails and footpaths where

  vegetation has been stressed by knocking down or foot stomping [34] [19].

- Vogelmann Red Edge 1 (VNIR-only & VNIR/SWIR)

$$VOGI = \frac{740\mu m}{720\mu m}$$

Equation 5: VOGI1 [47]

- The two effects of interest here are the foliage chlorophyll concentration, and the water content. Trails and footpaths littered with dead or stressed vegetation would show little signs of water content and low foliage chlorophyll concentrations. The VOGI1 filter showed promising signs of trail detection [47] [19].

- Cellulose Absorption Index (SWIR-only & VNIR/SWIR)

$$CAI = \frac{1}{2}(2.00\mu m + 2.20\mu m) - (2.10\mu m)$$

Equation 6: CAI [15]

- The CAI is the only index chosen that involves the use of entirely SWIR bands. The primary use of the CAI is to expose dry plant material. This formula can be used for finding trails that are a result of stressed vegetation in areas where vegetation is predominantly healthy. In this part of the SWIR spectrum, if there is stressed vegetation, a spectral absorption feature is observed with a minimum at 2.10 µm [15] [19].

- Normalized Difference Infrared Index (VNIR/SWIR)

$$NDII = \frac{0.819\mu m - 1.649\mu m}{0.819\mu m + 1.649\mu m}$$

Equation 7: NDII [24]

- The NDII is useful for the detection of changing water content within

    plant canopies and can be used for vegetation stress detection. These

    factors make it appropriate for detecting trails that may contain stressed

    vegetation. Moreover, this is one of two filters that involve the use of two

    regions of the spectrum simultaneously: the VNIR and the SWIR [24]

    [19].

- Moisture Stress Index (VNIR/SWIR)

$$MSI = \frac{1.599\mu m}{0.819\mu m}$$

Equation 8: MSI [13]

- This formula provides a measure of the water content of vegetation. There

    is an absorption for water in the spectrum at 1.599 μm. Vegetation

    containing more water, which is a sign of health, will have a deeper

    absorption at 1.599 μm [13] [19].

MaRS HSI and LiDAR Pixel Level Fusion

With respect to the American sweetgum tree analysis, once each of the five HSI

filters were calculated using the American sweetgum training ROIs shown in Figure 14

for each of the VNIR, SWIR, and VNIR/SWIR MaRS HSI cubes, the five filter planes

could be stacked into a single image using the "Layer Stacking" function in ENVI®. For

the trails analysis, this was accomplished the same way using the trails training ROIs

shown in Figure 15; however in accordance with Table 7, the number of HSI filters that

were used in the stacked HSI filter image varied for the trails analysis. The VNIR-only stacked HSI filter image was a 10-band filter image cube, the SWIR-only a 6-band image cube, while the VNIR/SWIR a 12-band image cube. As with any image cube (HSI or otherwise), a Z-profile can be displayed for each pixel in the cube, including the filter-only image cubes. These filter-only image cubes, however, can be considered images in the filter space, where spectral values are no longer representing ground reflectance; rather they are representing filter space values.

Moreover, the LiDAR transformation plane images could be appended onto the stack of HSI filter planes to form a 13-band HSI filter plus LiDAR transformation image cube for the sweetgum analysis in which each of the bands is scaled between 0 and 1. Figure 16 shows an example of an ENVI® screen capture of the stacked image in the ENVI® "Available Bands List," which includes georeferencing information. In this example, processing was completed on the SWIR-only HSI data and fused with the 8 LiDAR transformations. For the trails analysis, the filter + transformation image cubes varied in size with the VNIR-only image cube containing 23 total filter and transformation bands, the SWIR-only image 19 total filter and transformation bands, and the VNIR/SWIR having 25 total filter and transformation bands. Using these multi-band cubes, the same training ROIs shown in Figure 14 and Figure 15 could be used to apply additional filtering. With all of these multi banded images scaled between 0 and 1, each pixel formed a signature in the filter space. An example of a signature in this filter space could indicate where a pixel within the scene had a maximum height of, for example, 5 meters, but according to the filter planes from the HSI, did not match the target of

interest. Figure 17 shows a fused HSI filter and LiDAR transformation image cube from the sweetgum analysis where the red band is displaying height information from the LiDAR data (brighter red indicates taller vegetation), the green band is displaying the MTMF SWIR-only filter plane (brighter green indicates higher MTMF values for American sweetgum), and the blue band is displaying the SAM PC-rotated SWIR-only filter plane (brighter blue indicates a better SAM match). Generally, darker values in the image, especially black areas, denote areas where there is little to no match at all for the American sweetgum. Light areas, such as those that appear white or cyan, denote areas where all three of the image planes have high values, which indicates detections for the American sweetgum. Three additional filters were applied to this 13-band American sweetgum filter cube, which would be considered the final filter results for this part of the process: MF, ACE, and SAM.

Figure 18 shows a fused HSI filter and LiDAR transformation image of the trails analysis where the red band is displaying bare earth absolute roughness information from the LiDAR data (brighter red indicates rougher bare earth area), the green band is displaying the CAI filter plane available from the MaRS SWIR data (brighter green indicates lower CAI values, which can correspond to areas where these types of trails are established), and the blue band is displaying the MSI filter plane (brighter blue indicates areas that contain less water overall). Darker values in the image, especially black areas, denote areas where there is little to no match at all for the trails or footpaths. Light areas, such as those that appear white or cyan, denote areas where all three of the image planes have high values, which could indicate possible detections trails, but more generally,

areas of stressed vegetation and flat bare earth. This is an important point because, in the case of these trails, not all of the brighter white or cyan values necessarily indicate trails; rather, they merely indicate areas of stressed vegetation and flatter bare earth. The trails can be easily identified through quick visual inspection of the three color image planes shown in Figure 18. Although many linear features colored cyan and white are trails, some of these features are simply areas of bare earth. Some bare earth features are similar to trails and caused by excessive foot traffic, while other bare earth features are naturally occurring. Similar to the sweetgum analysis, three additional filters comprised of MF, ACE, and SAM results were applied to these multi banded image cubes.

This additional filtering amounts to one of three fusion experiments that would be performed. The second experiment was to take either the 8 LiDAR transformations from the sweet gum analysis or the 13 LiDAR transformations from the trails analysis and perform a layer stacking directly with the each of the original VNIR, SWIR, and VNIR/SWIR warped HSI cubes. For the sweetgum analysis, each of the VNIR and SWIR HSI files would increase from 125 bands to 133 bands with the inclusion of the LiDAR transformations, while the full VNIR/SWIR HSI file from the sweetgum analysis would increase from 250 bands to 258 bands with the inclusion of the LiDAR transformations. For the trails analysis, each of the VNIR and SWIR HSI files would increase from 125 bands to 138 bands with the inclusion of the LiDAR transformations, while the full VNIR/SWIR HSI file from the trails analysis would increase from 250 bands to 263 bands with the inclusion of the LiDAR transformations.

The third experiment was to simply compare the results of the MF, ACE, and SAM algorithms run solely on the MaRS HSI data with no incorporation of LiDAR data transformations or HSI filters. Reasons for choosing to only use the MF, ACE, and SAM for the final filtering included the following: A PC-rotated SAM requires a PCA transform and MTMF requires a MNF transform. Running PCA and MNF operations on HSI-only data and HSI plus LiDAR transformation data is an option that should be explored further. However, running PCA and MNF transforms on filter-only data (i.e., multi banded filter and transformation images) may not be appropriate, and warrants future investigation. Some reasons include, for example, the MNF transform attempts to estimate sensor noise. Estimating sensor noise from already filtered and transformed data does not seem sensible since some level of additional noise or error not attributed to sensor noise (such as anomalous MF pixels) could have been introduced by the filters. Since the PCA and MNF transforms were not processed for any of the experiments that involved only the multi banded filter and transformation image cubes, it was decided to set these algorithms aside for the final filtering process for consistency. Table 6 illustrates each of the experiments along with the filters, transformations, and bands used throughout the sweetgum exercise while Table 7 illustrates each of the experiments along with the filters, transformation, and bands used throughout the trails exercise.
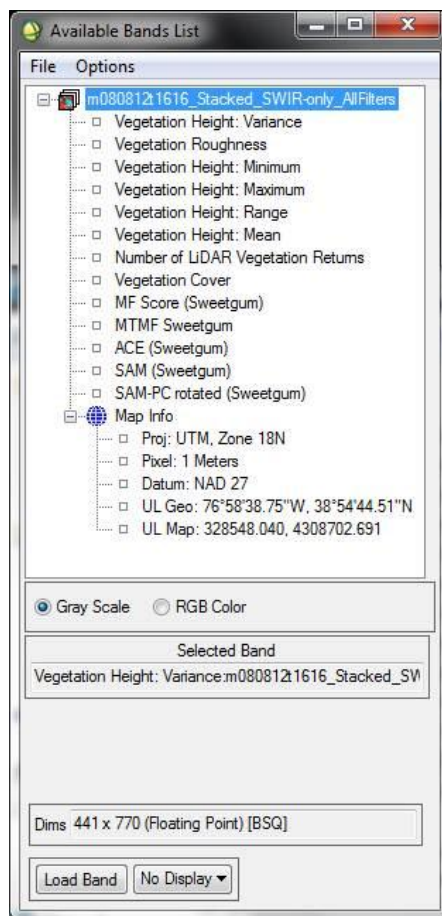
**Figure 16: Stacked HSI (SWIR-only) filter and LiDAR transformation image cube as displayed in the ENVI®
"Available Bands List" window.**

Table 6: HSI and LiDAR fusion experiments performed for the American sweetgum analysis. The "HSI Filters" column refers to the five HSI filters that were included in the 13 band layer stacked filter and transformation image cube. The "Final Filters" column refers to the three filters that were performed on the final fused images. For consistency, the same three final filters were used on every fused (or non-fused) image. Color has been added to the table for visual clarity. Light green represents the VNIR-only experiments, light blue represents the SWIR-only experiments, and light orange represents the full VNIR/SWIR experiments.

American sweetgum Experiments				
Experiment	**Bands Used**	**5 HSI Filters**	**Total Number of Bands in Image Cube**	**Final Filters**
1.1	8 LiDAR Vegetation + 5 HSI filters (VNIR-only)	MF, MTMF, ACE, SAM, SAM PC-rotated	13	MF, ACE, SAM
1.2	8 LiDAR Vegetation + 125 HSI spectral bands (VNIR-only)	N/A	133	MF, ACE, SAM
1.3	125 HSI Spectral Bands Only (VNIR-only)	N/A	125	MF, ACE, SAM
2.1	8 LiDAR Vegetation + 5 HSI filters (SWIR-only)	MF, MTMF, ACE, SAM, SAM PC-rotated	13	MF, ACE, SAM
2.2	8 LiDAR Vegetation + 125 HSI spectral bands (SWIR-only)	N/A	133	MF, ACE, SAM
2.3	125 HSI Spectral Bands Only (SWIR-only)	N/A	125	MF, ACE, SAM
3.1	8 LiDAR Vegetation + 5 HSI filters (VNIR/SWIR)	MF, MTMF, ACE, SAM, SAM PC-rotated	13	MF, ACE, SAM
3.2	8 LiDAR Vegetation + 250 HSI spectral bands (VNIR/SWIR)	N/A	258	MF, ACE, SAM
3.3	250 HSI Spectral Bands Only (VNIR/SWIR)	N/A	250	MF, ACE, SAM

Table 7: HSI and LiDAR fusion experiments performed for the trails / footpaths analysis. The "HSI Filters" column refers to the 12 total HSI filters that were included with the 13 LiDAR transformations in either the 22-band layer stacked VNIR-only filter image cube, the 19-band layer stacked SWIR-only image cube, or the 25-band layer stacked VNIR/SWIR image cube. The "Final Filters" column refers to the three filters that were performed on the final fused images. For consistency, the same three final filters were used on every fused (or non-fused) image. Color has been added to the table for visual clarity. Light green represents the VNIR-only experiments, light blue represents the SWIR-only experiments, and light orange represents the full VNIR/SWIR experiments.

Trails / Footpaths Experiments				
Experiment	Bands Used	HSI Filters Used	Total Number of Bands in Image Cube	Final Filters
4.1	8 LiDAR Vegetation & 5 Bare Earth + 10 HSI filters (VNIR-only)	MF, MTMF, ACE, SAM, SAM PC-rotated, ARVI, SR, SIPI, VOGI1	23	MF, ACE, SAM
4.2	8 LiDAR Vegetation & 5 Bare Earth + 125 HSI spectral bands (VNIR-only)	N/A	138	MF, ACE, SAM
4.3	125 HSI Spectral Bands Only (VNIR-only)	N/A	125	MF, ACE, SAM
5.1	8 LiDAR Vegetation & 5 Bare Earth + 6 HSI filters (SWIR-only)	MF, MTMF, ACE, SAM, SAM PC-rotated, CAI	19	MF, ACE, SAM
5.2	8 LiDAR Vegetation & 5 Bare Earth + 125 HSI spectral bands (SWIR-only)	N/A	138	MF, ACE, SAM
5.3	125 HSI Spectral Bands Only (SWIR-only)	N/A	125	MF, ACE, SAM
6.1	8 LiDAR Vegetation & 5 Bare Earth + 12 HSI filters (VNIR/SWIR)	MF, MTMF, ACE, SAM, SAM PC-rotated, ARVI, CAI, MSI, NDII, SR, SIPI, VOGI1	25	MF, ACE, SAM
6.2	8 LiDAR Vegetation & 5 Bare Earth + 250 HSI spectral bands (VNIR/SWIR)	N/A	263	MF, ACE, SAM
6.3	250 HSI Spectral Bands Only (VNIR/SWIR)	N/A	250	MF, ACE, SAM

Figure 17: Fused HSI and LiDAR transformation image cube example. Brighter values such as those that appear white or cyan denote areas of possible detections for the American sweetgum tree. Darker areas, such as those that appear black, denote areas where the filter and transformation planes are displaying prominently low values. Areas that are of a single color red, green, or blue, denote areas where only one of the filters or transformations was returning higher values.
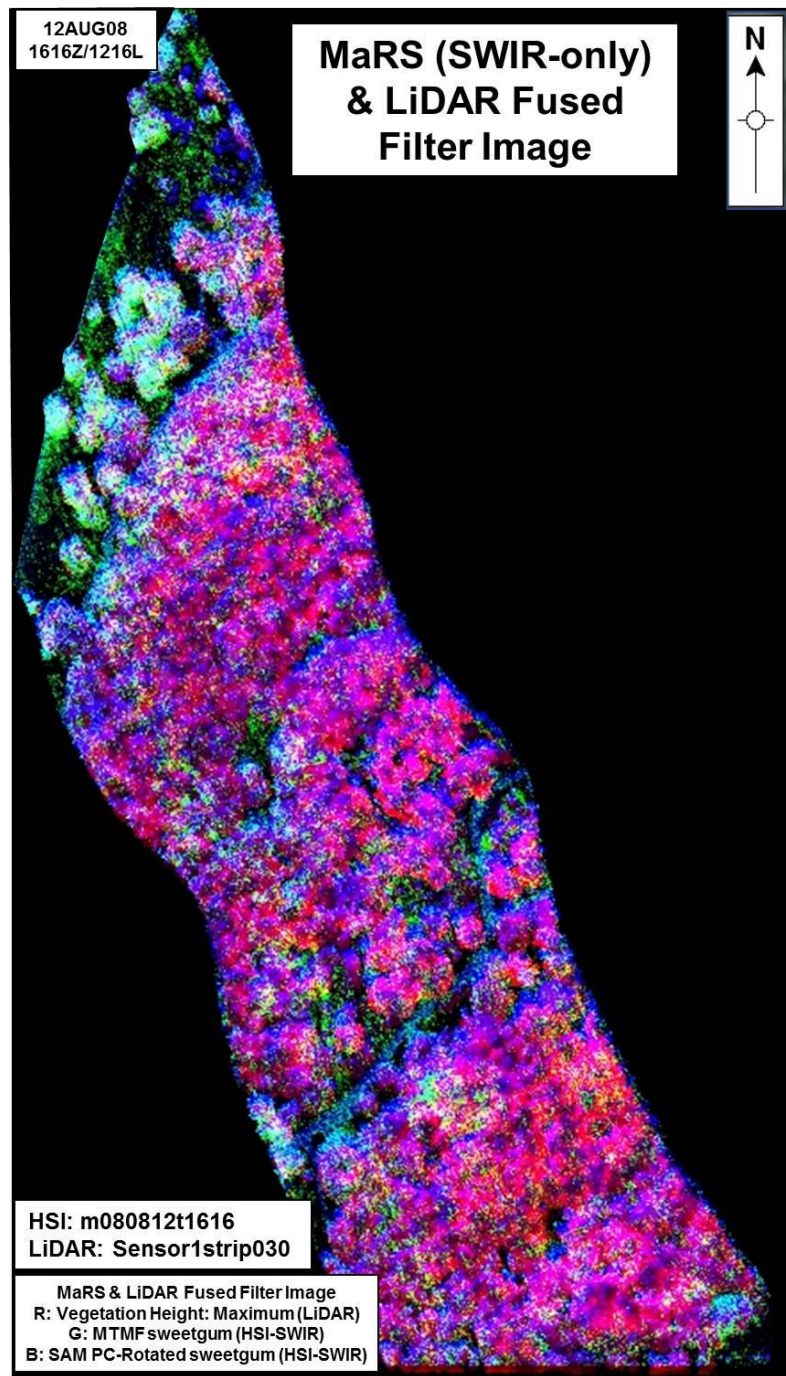
Figure 18: Fused HSI and LiDAR transformation image cube example. Brighter values such as those that appear white or cyan denote areas of possible detections for trails and footpaths, but could also indicate bare soil and stressed vegetation. Darker areas, such as those that appear black, denote areas where the filter or transformation planes are displaying prominently low values. Areas that are of a single color red, green, or blue, denote areas where only one of the filters or transformations was returning higher values.
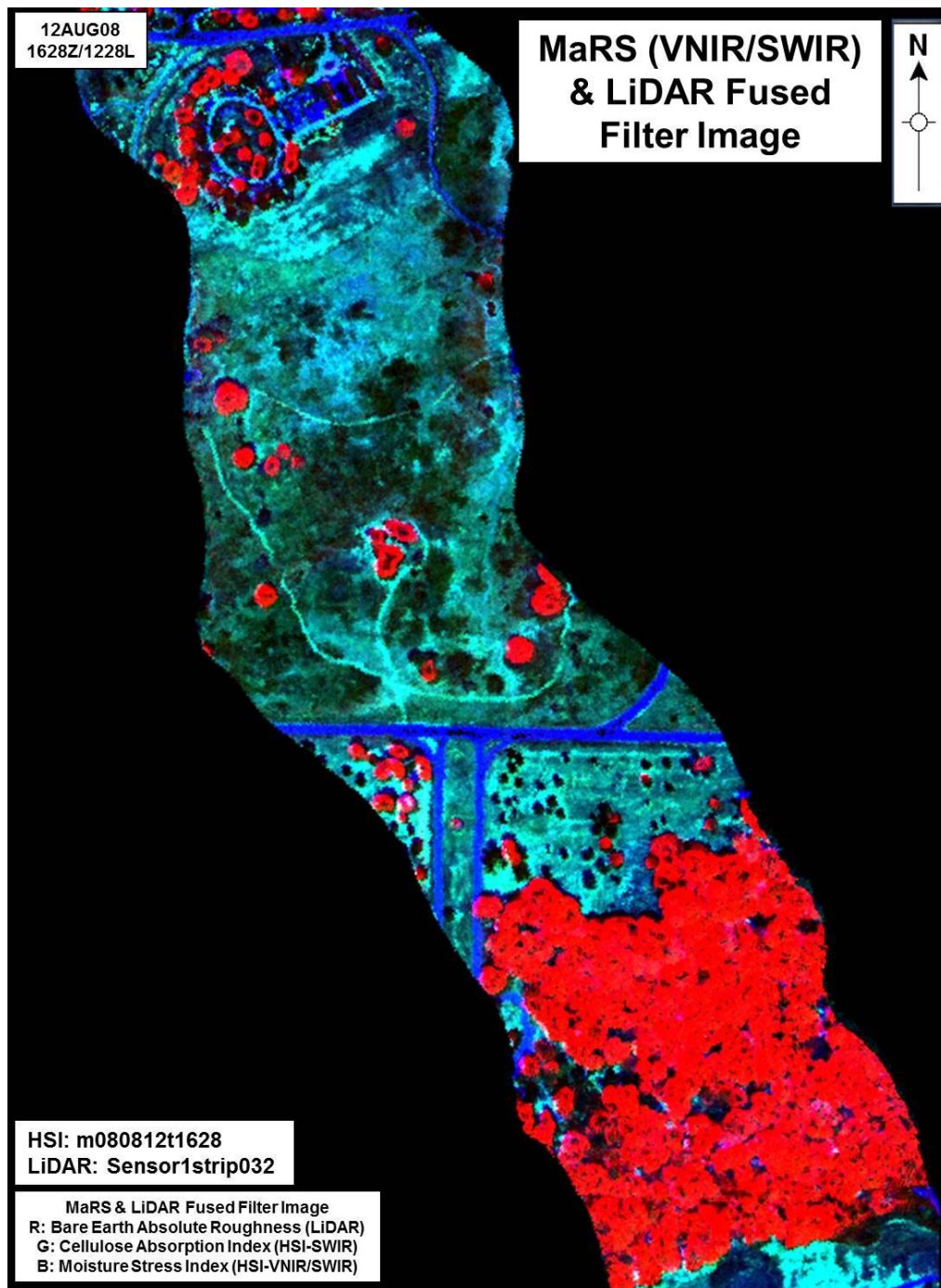
Receiver Operator Characteristic (ROC) Curve Generation

The last step of this process was to evaluate the performance of each of the final

filters and compare their performance. This evaluation was completed by generating

ROC curves for each of the final filter planes. The "ROC Curves" function in ENVI® was

used to execute this process. Prior to generating the ROC curves, ground truth ROIs had

to be created for both the American sweetgum analysis and also the trails analysis. For

the American sweetgum analysis, true color MaRS images and LiDAR vegetation

roughness images were visually compared to the ground truth maps in ArcGIS®

concurrently, and those pixels that represented American sweetgum trees were manually

identified. Figure 19 shows the ground truth ROI that was manually selected. For the

trails analysis, true color and SWIR color composite MaRS images were displayed and

compared with the high resolution USGS orthoimagery in order to manually identify the

location of the trails of interest. Additionally, some of the HSI filter planes, such as the

CAI were useful in initially separating the trails from the background. Figure 20 shows

the trails ground truth ROI that was manually selected. As of August 3rd, 2012, all of the

trails depicted in Figure 20 by ROIs remained in the same location. As mentioned,

earlier, however, the trails appear to be in better condition in 2012 with less foot traffic

and/or covered with healthier (less stressed) foliage.

Using the ground truth ROI, ROC curves could be generated. It is important to

note that, for consistency in the ROC curves, the final filter planes for the SAM images

had to be inverted using the software provided by Dr. Ronald Resmini. This inversion

had to take place so that higher values in the SAM filter planes represented better

detection results like the MF and ACE filter planes. This was similar to what occurred

prior to the HSI filter stacking. Each ROC curve contained 100 points for smoothness

with the Probability of detection (P_d) on the y-axis and the Probability of false alarm (P_f)

on the x-axis.

Finally, single metric had to be used in order to compare the ROC curves. This

could be achieved by calculating the area under each of the ROC curves, or more simply

the area under the curve (AUC). More area under a ROC curve indicates a better

performance because this would account for a higher P_d and a lower P_f. This integration

was performed using the Trapezoidal rule, uniform method, which is one of the most

straightforward ways to calculate the AUC [11]. The following equation was used:

$$\int_a^b f(x)dx = \frac{1}{2}\sum_{i=1}^{N}(X_{i+1} - X_i)(f(X_{i+1}) + f(X_i))$$

Equation 9: Trapezoidal rule (non-uniform grid) as implemented

In Equation 9, "*i*" refers to each ROC curve sampling interval, "*N*" refers to the total

number of steps or samples (100), while "*X*" refers to the P_f value and "*f(X)*" refers to the
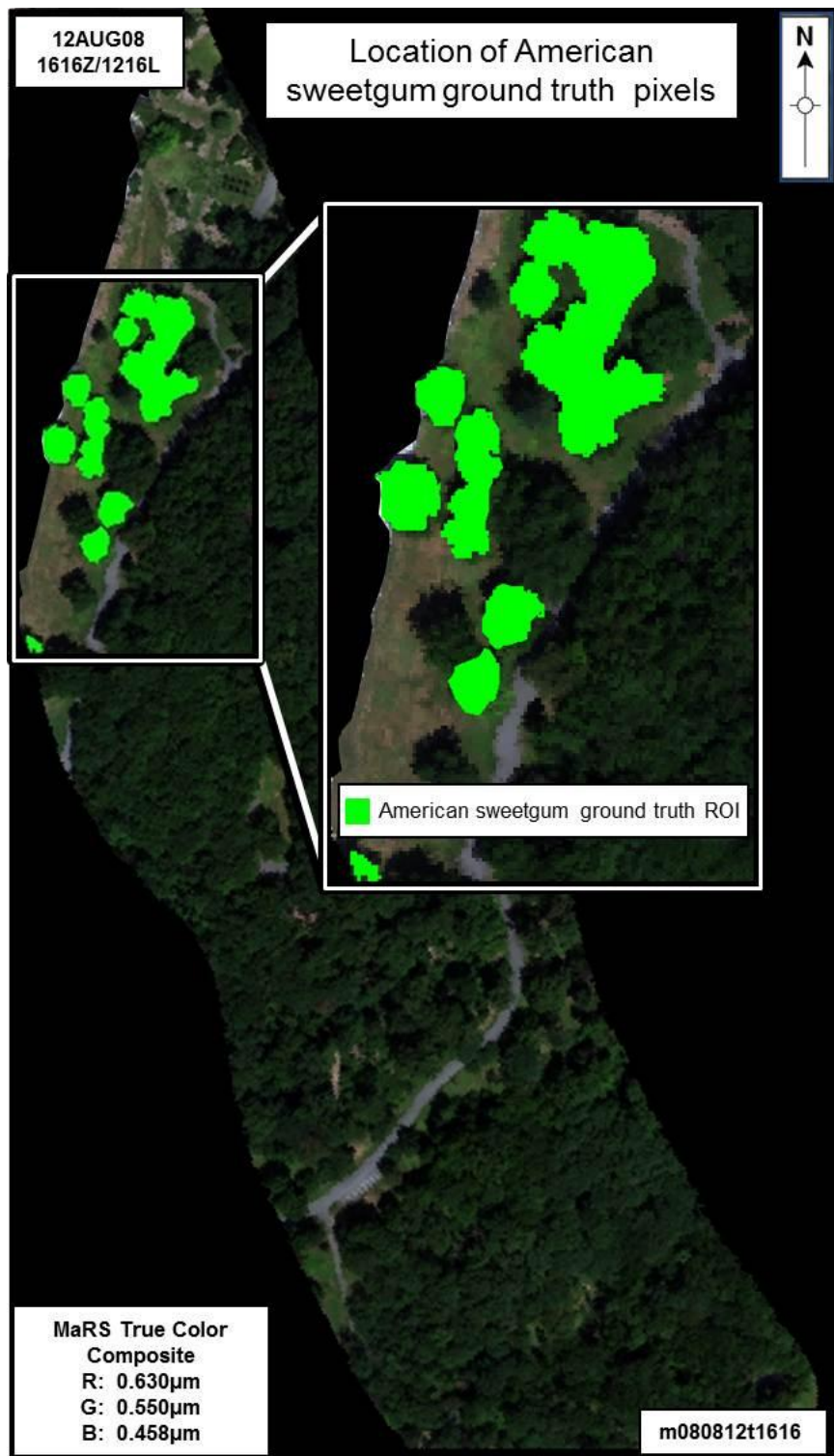
P_d value.

Figure 19: American sweetgum ground truth ROIs.

Figure 20: Trails ground truth ROIs.

RESULTS AND DISCUSSION

In this section, the American sweetgum results will be presented followed by the trails results. Results will include ROC curves and AUC charts, which will demonstrate the performance of the fusion process and the algorithms used throughout this process.

American sweetgum VNIR, SWIR, and VNIR/SWIR Analysis

Figure 22 through Figure 24 show the ROC curve results for the American sweetgum analysis. Table 10 shows the final AUC results for all of the sweetgum ROC curves. The table has been color coded for easier visual interpretation. Arbitrary threshold values of less than 0.90, between 0.90 – 0.93, and greater than 0.94 were established for the color coding. By simple visual inspections of the ROC curves, the MF performed the best out of the three final algorithms. Objectively, the MF algorithm had the most consistent AUC performance metric at 0.94 for seven out of the nine total sweetgum experiments. The MF algorithm performed the worst for the full VNIR/SWIR filters only experiment 3.1 with an AUC value of 0.89 while the SAM algorithm performed the best in experiment 3.1 with an AUC value of 0.93. Interestingly, the SAM algorithm performs the worst overall for the sweetgum experiments with seven of the nine AUC values under 0.90. This could mean that the spectral signature of the sweetgum tree is more unique from the background vegetation than originally anticipated. It was hypothesized that the sweetgum ground truth signature would be mixed into background statistics used to build

75

the MF and ACE kernels, and that the demeaning step of data whitening would negatively impact the performance of algorithms such as MF and ACE. Since these negative impacts are not observed as originally anticipated, the sweetgum signature may present some unique qualities, which could warrant further investigation to those interested in such analysis.

Additionally, the three most consistently large performance gaps occur between the MF and SAM algorithms for the full HSI + LiDAR transformations experiments 1.2, 2.2, and 3.2. The MF performed 13% better in experiments 1.2 and 2.2, while the MF performed 16% better in experiment 3.2. In experiment 3.2, although the AUC value for MF was consistent with experiments 1.2 and 2.2 with a value of 0.94, the SAM value was lower with a value of 0.81. The largest gap, however, was in SWIR-only, HSI-only experiment 3.3 where the MF performed 18% better than did the SAM. This result alone indicates unique differences between the SWIR portions of the sweetgum reflectance spectrum from other SWIR spectra making up the background.

Also regarding SWIR-only values, it is surprising to see that some of the algorithms for the SWIR-only experiments 2.1 − 2.3 outperformed some of the VNIR-only experiments 1.1 − 1.3. The filters-only SWIR-only ACE experiment 2.1 performed 5% better than the filters-only VNIR-only ACE experiment 1.1. Moreover, the filters-only SWIR-only SAM experiment 2.1 performed 4% better than the filters-only VNIR-only SAM experiment 1.1. This is surprising since one of the key factors typically used for vegetation discrimination is the red-edge portion of the spectrum, which resides in the VNIR.

Something that should not be overlooked is the overall general performance of the

filters and transformation-only experiments 1.1, 2.1, and 3.1 where the AUC values are

comparable to the rest of the experiments with only minor variations. In some

experiments such as the SAM SWIR-only experiments 2.1 – 2.3, the filters and

transformation -only experiment 2.1 outperformed the HSI + LiDAR and HSI-only

experiments 2.2 and 2.3 by factors of 12% and 16%. The same occurs for the full

VNIR/SWIR experiments 3.1 – 3.3 where the SAM filters and transformations-only

experiment 3.1 outperforms the HSI + LiDAR and HSI-only experiments 3.2 and 3.3 by

factors of 15% and 9%. Moreover, for the VNIR-only MF experiments 1.1 – 1.3, the

filters and transformations-only experiment 1.1 has the same performance as the HSI +

LiDAR and HSI-only experiments 1.2 and 1.3 with an AUC value of 0.94. The reason

this is fascinating is because the filters and transformations-only image cubes are only

comprised of 13 bands, which by data size, is orders of magnitudes smaller than the size

of a full HSI data cube.

The reason these filters-only image cubes present comparable–and in some cases

better–results can be attributed to many of the filter bands being uncorrelated. It is

generally understood that HSI image cubes containing more uncorrelated bands allows

for the extraction of more information [41]. Using a 13-band filter image cube from the

American sweetgum SWIR-only experiment 2.1, a correlation matrix was generated. The

correlation matrix is shown in Table 8. It makes sense that many of the LiDAR

transformations show high correlation since many of the filters are calculated in a similar

fashion. It also makes sense that the LiDAR transformations do not show correlation to

the HSI filters, which is why more information can be extracted from these filters when they are fused. Moreover, there is higher correlation between the MF, MTMF, and ACE HSI filters, which can be expected because these filters are similar. However, the impact that correlation has on the results presented here requires additional consideration.

Table 8: A correlation matrix of the 13-band filter image cube used in American sweetgum experiment 2.1; values > 0.75 are color coded red and represent high correlation, while values > 0.50 > 0.75 are color coded yellow and represent medium correlation, and values < 0.50 are color coded green and show low correlation.

Band (Filter)	Vegetation Cover	Number of LiDAR Vegeation Returns	Vegetation Height: Mean	Vegetation Height: Range	Vegetation Height: Maximum	Vegetation Height: Minimum	Vegetation Roughness	Vegetation Height: Variance	ACE Sweetgum	MTMF Sweetgum	SAM Sweetgum	SAM PC-Rotated Sweetgum	MF Sweetgum
Vegetation Cover	1.00	0.84	0.86	0.37	0.84	0.75	0.33	0.13	0.42	0.22	0.69	0.55	0.14
Number of LiDAR Vegeation Returns	0.84	1.00	0.73	0.44	0.75	0.59	0.36	0.18	0.37	0.20	0.59	0.48	0.12
Vegetation Height: Mean	0.86	0.73	1.00	0.38	0.96	0.89	0.35	0.20	0.38	0.17	0.61	0.50	0.08
Vegetation Height: Range	0.37	0.44	0.38	1.00	0.59	0.04	0.97	0.88	0.21	0.14	0.33	0.28	0.09
Vegetation Height: Maximum	0.84	0.75	0.96	0.59	1.00	0.78	0.57	0.41	0.39	0.19	0.62	0.51	0.10
Vegetation Height: Minimum	0.75	0.59	0.89	0.04	0.78	1.00	0.05	0.18	0.32	0.12	0.51	0.42	0.06
Vegetation Roughness	0.33	0.36	0.35	0.97	0.57	0.05	1.00	0.92	0.20	0.13	0.31	0.27	0.09
Vegetation Height: Variance	0.13	0.18	0.20	0.88	0.41	0.18	0.92	1.00	0.11	0.07	0.17	0.14	0.04
ACE Sweetgum	0.42	0.37	0.38	0.21	0.39	0.32	0.20	0.11	1.00	0.73	0.45	0.37	0.63
MTMF Sweetgum	0.22	0.20	0.17	0.14	0.19	0.12	0.13	0.07	0.73	1.00	0.24	0.28	0.94
SAM Sweetgum	0.69	0.59	0.61	0.33	0.62	0.51	0.31	0.17	0.45	0.24	1.00	0.42	0.14
SAM PC-Rotated Sweetgum	0.55	0.48	0.50	0.28	0.51	0.42	0.27	0.14	0.37	0.28	0.42	1.00	0.14
MF Sweetgum	0.14	0.12	0.08	0.09	0.10	0.06	0.09	0.04	0.63	0.94	0.14	0.14	1.00

One last analysis was conducted to determine if the different algorithm methods identified different pixels within the ground truth ROIs. Only experiment 3.1–full VNIR/SWIR HSI filters and LiDAR transformations–was selected for this analysis. Algorithm results were based on an arbitrary P_f threshold of 0.10. Using a logical combination of the algorithm results detailed in Table 9, it was determined that the different detection methods do identify different pixels; this is shown in Figure 21. The blue ROIs shown in Figure 21 represent the pixels added by the SAM and ACE algorithms. Although it appears as though the SAM and ACE algorithms added the most pixels, each of the green and red pixels shown in Figure 21are pixels that have been added by the other two algorithm combinations in addition to the SAM and ACE algorithm combination. As an example, including a MF with the SAM instead of an ACE

with the SAM showed a 7% improvement in detection based on the arbitrary P_f threshold

of 0.10.

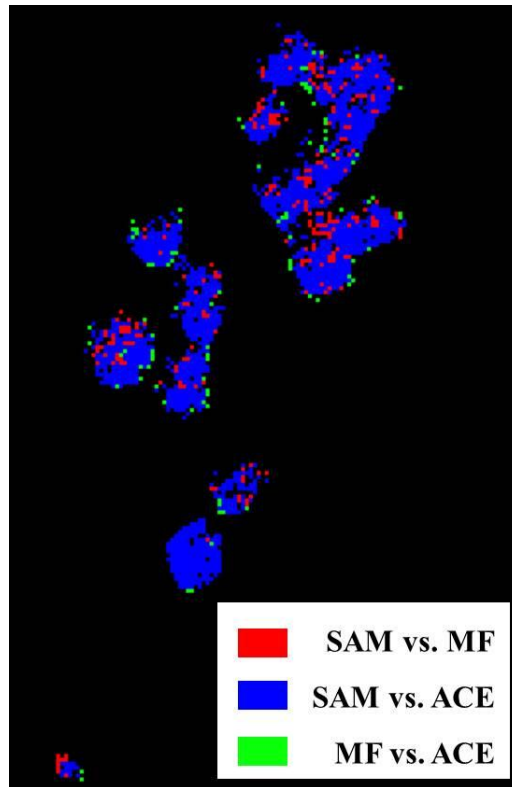| Filter Analysis Based On PF_a Threshold of 10%		
Filters	# of Ground Truth Pixels Detected	Percent of Ground Truth Pixels Detected (Total Ground Truth Pixels = 3,289)
SAM vs MF	1916	58%
SAM vs ACE	1693	51%
MF vs ACE	1756	53%

Figure 21: A graphical display of the filter comparison analysis for experiment 3.1. The analysis was completed only on the American sweetgum ground truth pixels to determine the number of target pixels detected by each combination of algorithms outlined in Table 9.
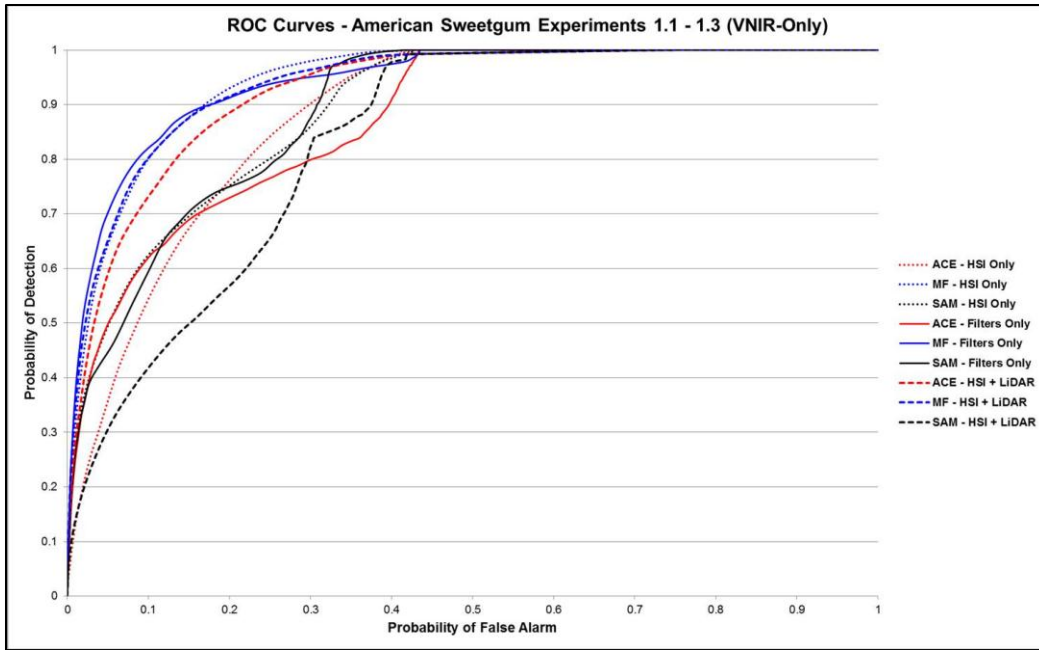
Figure 22: ROC curves representing American sweetgum experiments 1.1 - 1.3 (VNIR-only)
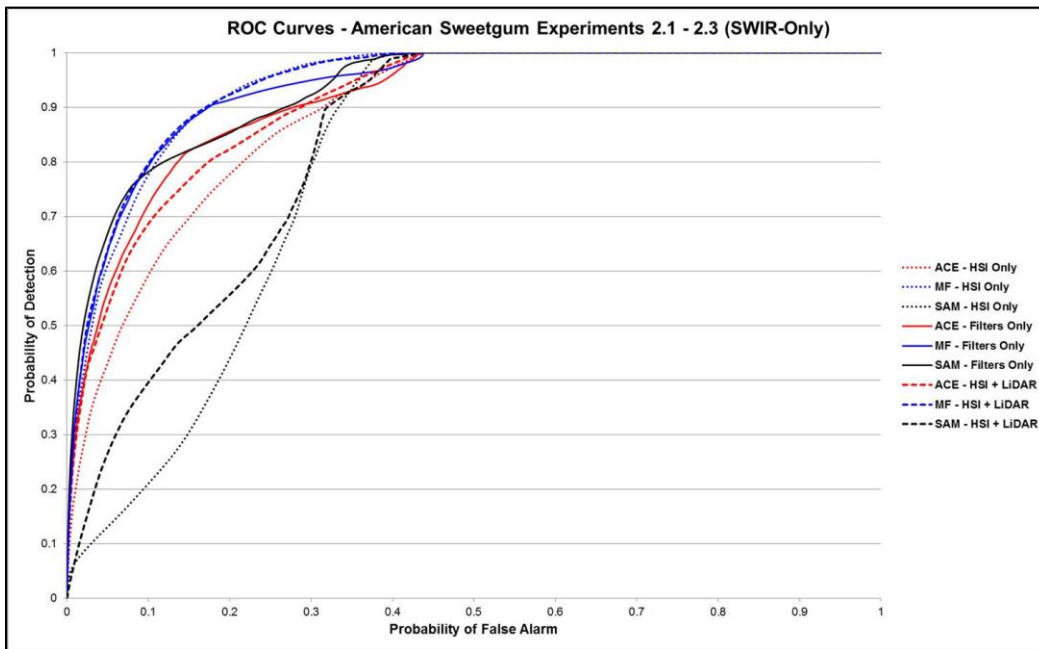

Figure 23: ROC curves representing American sweetgum experiments 2.1 - 2.3 (SWIR-only)
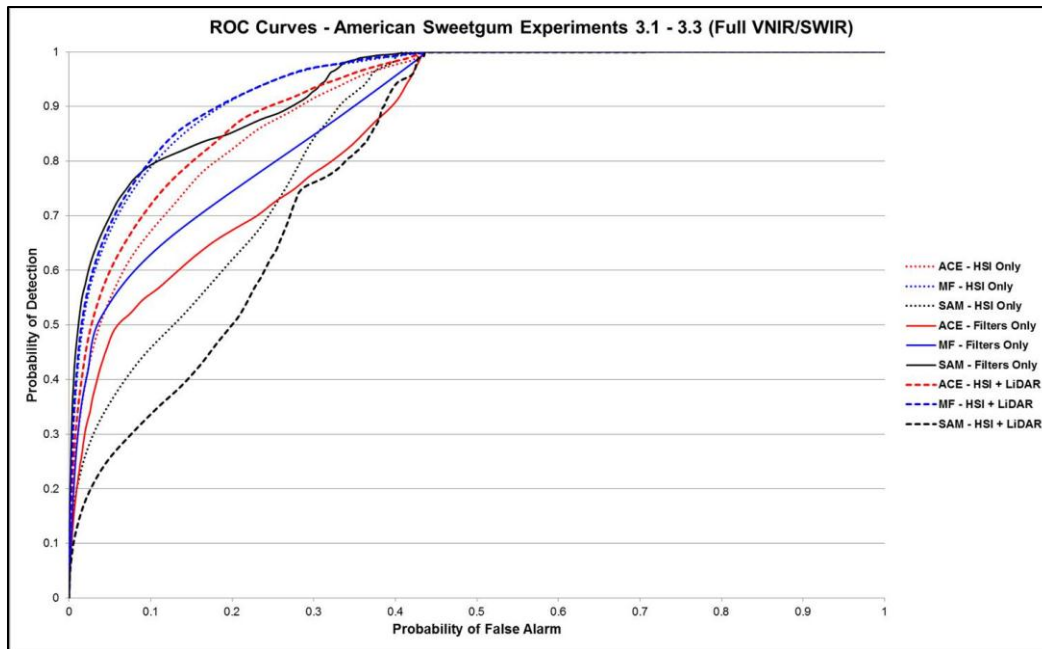
Figure 24: ROC curves representing American sweetgum experiments 3.1 - 3.3 (Full VNIR/SWIR)

Table 10: Final American sweetgum AUC results. For ease of visual analysis, values less than 0.90 are color coded red, values between 0.90 and 0.93 are color coded yellow, and values equal to or above 0.94 are color coded green. Higher numbers indicate a better performance where 0 is the minimum and 1 is the maximum.

Experiment	Bands Used	Final ACE AUC Value	Final MF AUC Value	Final SAM AUC Value
1.1	8 LiDAR Vegetation + 5 HSI filters (VNIR-only)	0.87	0.94	0.89
1.2	8 LiDAR Vegetation + 125 HSI spectral bands (VNIR-only)	0.92	0.94	0.83
1.3	125 HSI Spectral Bands Only (VNIR-only)	0.88	0.94	0.89
2.1	8 LiDAR Vegetation + 5 HSI filters (SWIR-only)	0.91	0.93	0.93
2.2	8 LiDAR Vegetation + 125 HSI spectral bands (SWIR-only)	0.91	0.94	0.83
2.3	125 HSI Spectral Bands Only (SWIR-only)	0.89	0.94	0.80
3.1	8 LiDAR Vegetation + 5 HSI filters (VNIR/SWIR)	0.86	0.89	0.93
3.2	8 LiDAR Vegetation + 250 HSI spectral bands (VNIR/SWIR)	0.92	0.94	0.81
3.3	250 HSI Spectral Bands Only (VNIR/SWIR)	0.91	0.94	0.85

Trails and Footpaths VNIR, SWIR, and VNIR/SWIR Analysis

Figure 25 through Figure 27 show the ROC curve results for trails analysis. Table 11 shows the final AUC results for the trails ROC analysis. Similar to the sweetgum analysis, the table has been color coded for easier visual interpretation. Like the sweetgum analysis, values less than 0.90, between 0.90 – 0.93, and greater than 0.94 were established for the color coding. Generally, algorithm performance for the trails analysis was quite different than the sweetgum analysis. According to Table 11, the SAM algorithm performed the best while the ACE algorithm performed the worst. On the contrary, for the sweetgum analysis, the ACE algorithm performed in the middle while

the SAM algorithm performed the worst. This may indicate that since the trails are comprised of mainly background vegetation and dirt materials, these materials are not standing out from the background like the sweetgum trees. As a result, for the ACE algorithm throughout, and for the filters and transformations-only MF experiments 5.1 and 6.1, the average spectral signature of the trails mixes in with the background vegetation spectra as originally anticipated. Consequently, the trails ground truth signature mixes into statistics used to build the MF and ACE kernels, and the demeaning step of data whitening negatively impacts the performance of the ACE algorithms throughout, and the MF algorithm for filters and transformations-only experiments 5.1 and 6.1.

Although slight, SAM algorithm performance trends upwards with added SWIR bands. Differences are no more than 1% - 2%. The largest AUC gaps for the trails analysis occur between the performance of the SAM algorithm and the ACE algorithm. For the full VNIR/SWIR experiments 6.2 (HSI + LiDAR) and 6.3 (HSI-only), the SAM algorithm performs 9% and 10% better respectively. As more bands of HSI and LiDAR transformation information are added for this non-unique trails problem, the performance of the ACE algorithm degrades. More bands of information are creating an overabundance of vegetation background, which is causing the trails ground truth signature to mix into the background statistics, and thus degrade overall ACE algorithm performance.

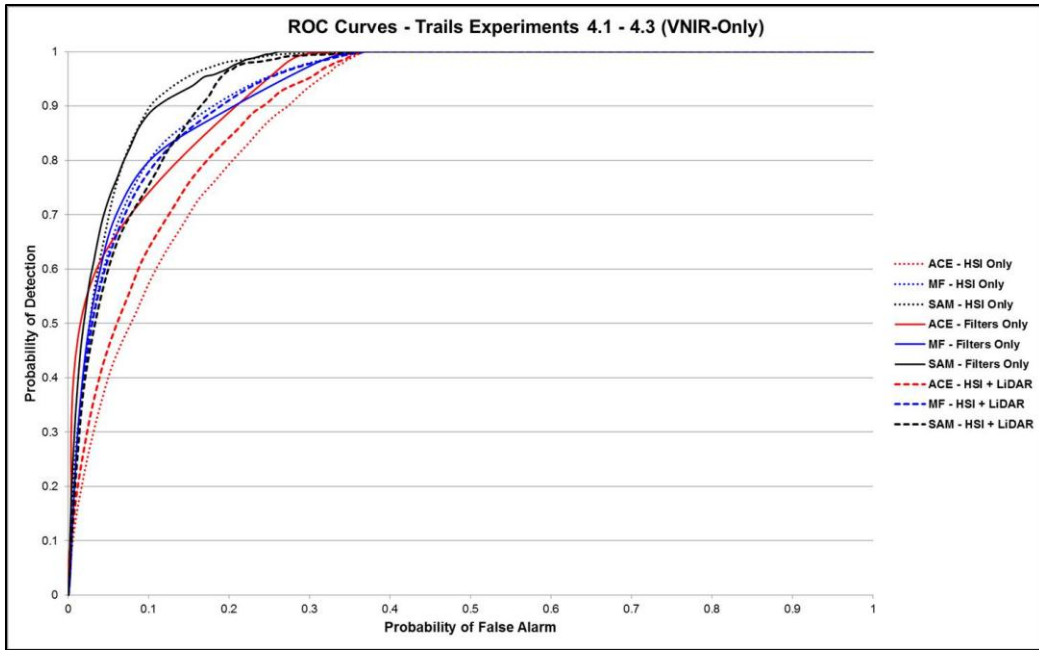**Figure 25: ROC curves representing trails experiments 4.1 - 4.3 (VNIR-only)**

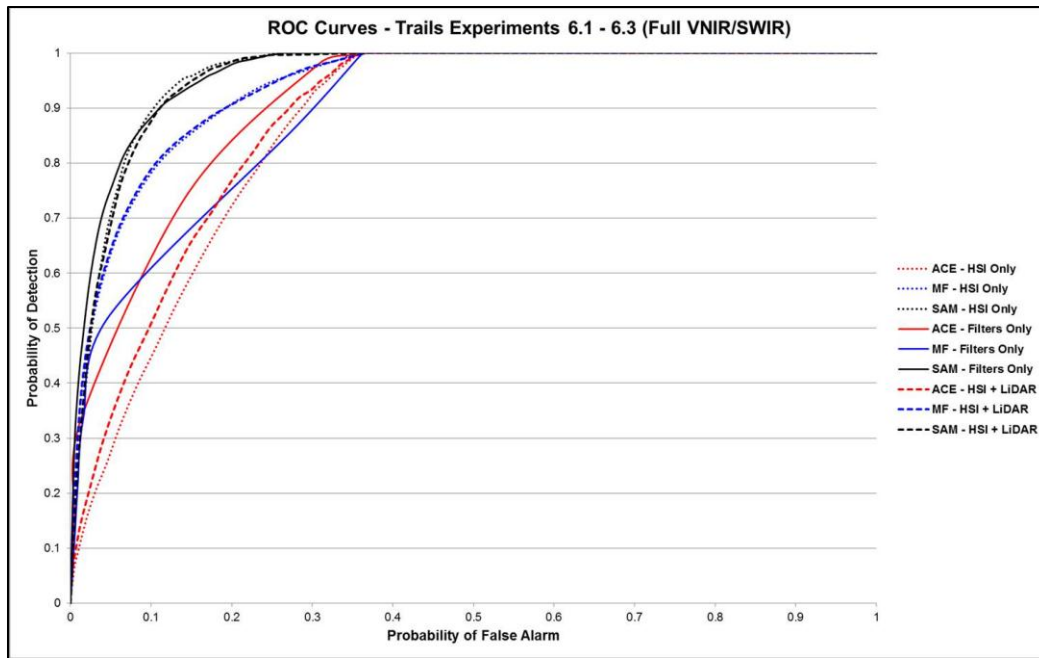**Figure 26: ROC curves representing trails experiments 5.1 - 5.3 (SWIR-only)**

Figure 27: ROC curves representing trails experiments 6.1 - 6.3 (full VNIR/SWIR)

Table 11: Final trails AUC results. For ease of visual analysis, values less than 0.90 are color coded red, values between 0.90 and 0.93 are color coded yellow, and values above 0.94 are color coded green. Higher numbers indicate a better performance where 0 is the minimum and 1 is the maximum.

Experiment	Bands Used	Final ACE AUC Value	Final MF AUC Value	Final SAM AUC Value
4.1	8 LiDAR Vegetation & 5 Bare Earth + 10 HSI filters (VNIR-only)	0.93	0.94	0.96
4.2	8 LiDAR Vegetation & 5 Bare Earth + 125 HSI spectral bands (VNIR-only)	0.91	0.94	0.94
4.3	125 HSI Spectral Bands Only (VNIR-only)	0.89	0.94	0.96
5.1	8 LiDAR Vegetation & 5 Bare Earth + 6 HSI filters (SWIR-only)	0.91	0.89	0.95
5.2	8 LiDAR Vegetation & 5 Bare Earth + 125 HSI spectral bands (SWIR-only)	0.91	0.94	0.95
5.3	125 HSI Spectral Bands Only (SWIR-only)	0.91	0.94	0.95
6.1	8 LiDAR Vegetation & 5 Bare Earth + 12 HSI filters (VNIR/SWIR)	0.91	0.89	0.96
6.2	8 LiDAR Vegetation & 5 Bare Earth + 250 HSI spectral bands (VNIR/SWIR)	0.88	0.94	0.96
6.3	250 HSI Spectral Bands Only (VNIR/SWIR)	0.87	0.94	0.96

CONCLUSION

Several conclusions and recommendations for future work can be derived from this project. The addition of information from the SWIR can be valuable for some cases of vegetation mapping throughout the HSI and LiDAR fusion process, but it remains inconclusive for others. Algorithm performance is effected by unique versus non-unique targets sets. The addition of SWIR for non-unique background vegetation enhanced results. Thus, if available, the SWIR should always be used, and not discarded, to enhance detection results on a case dependent basis.

In looking at the results section, the method chosen to measure the performance of the algorithms operating on the fused HSI and LiDAR data should probably be altered. Graphically, it appears that the results are there, especially in Figure 17 and Figure 18. Although no screen captures are provided here, when looking at raw MF and ACE filter planes, clumps of trees representing the American sweetgum are clearly visible to the eye, and the same goes for the trails analysis. The pixel-by-pixel ROC curve method of measuring performance is probably not appropriate for such high abundance targets like vegetation and background materials. Rather, these methods are good for low abundance targets and algorithm performance such as the classic example of finding plastic in a large body of water where the plastic would clearly stand out from the water background. Accordingly, object based methods as opposed to pixel based methods of measuring

performance may have been more appropriate here. For example, if there were 12 sweetgum trees in the scene or 4 trails in the scene, instead of counting the number of pixels that were detected and number false alarmed, simply counting the number of trees detected in general by identifying clumps of pixels that represent these types of large targets.

Next is the idea of low and high abundance target mapping, generally. High abundance targets were chosen for this exercise, which can in some cases be much more difficult to map with accuracy. For example, Mundt et al. (2006) had success in mapping sagebrush vegetation using HSI and LiDAR fusion, but this vegetation was in an arid region, and was therefore a low abundance target, which made it easier to map.

Furthermore, there were no efforts during this exercise to reduce data dimensionality. Some quick data dimensionality reduction tests were performed on the data used for this project, and some of the results were orders of magnitude better than the results shown in Table 10 and Table 11. The idea of reducing data dimensionality on fused HSI and LiDAR data could be a research topic alone. For example, does it make sense to reduce the data dimensionality of a fused HSI and LiDAR transformation s-only image such as those images presented in experiments 1.1, 2.1, 3.1, 4.1, 5.1, and 6.1? If so, how many filters and / or transformations should be included and by how much should the dimensionality be reduced? What are the thresholds of reduction? The same questions could be asked for an HSI image where the LiDAR transformations have been added as extra bands such as those in experiments 1.2, 2.2, 3.2, 4.2, 5.2, and 6.2. Although it was tempting to produce and present results from such data dimensionality reduced data sets,

true research should be completed in this respect, which is outside of the bounds of this project.

Additionally, the idea of data compression from stacked filter and transformation images was thought provoking. Given the amount of memory computers have now, raw data can technically be processed in the memories of computers without ever actually being stored. As seen in Table 10 and Table 11, the stacked filters and transformation-only images did almost as well, and in some cases better, than the full HSI images. Remarkably, these stacked filter and transformation images are only between 20Mb and 40Mb in size. The warped HSI images are all over 100Mb in size. In fact, some of the warped HSI images that also contain the added LiDAR transformation bands are over half a gigabyte in size. This goes to show that if filtering the final filter and transformation planes can produce equally or even better results, perhaps some of the original data can be discarded, or perhaps never stored to begin with if all of it was processed in the computer memory.

Finally, an alternative means of weighting or classifying the HSI and LiDAR transformation planes during pixel level fusion should be investigated. Using the LiDAR height transformation as the example, this transformation was simply added in as an additional band. Although this is not bad information, the height band is being interlaced with the rest of the filter and transformation planes and some of the information possibly lost. Perhaps there could be an option where this transformation is set specifically as a height plane, and each pixel is processed accordingly. In other words, if the user were looking for a type of vegetation with certain spectral characteristics that were at an exact

89

height of 5 meters above the ground, computer software such as ENVI® could recognize–

on a pixel level using a raster format within a multi banded file–which pixels are worthy

of processing and which ones are not based on this single band of information. This could

almost be viewed as a hybrid feature level and pixel level style of fusion. Other LiDAR

transformation planes, such as vegetation roughness or surface roughness could possibly

be treated the same way.

This project ends with 3D perspective views of the National Arboretum. Figure

28 and Figure 29 show the overall quality of the LiDAR data fused with the HSI data,

and in particular, the precision of the georegistration between the two datasets. The 3D

perspective views were generated using E3De™.

Figure 28: HSI and LiDAR 3D perspective view of the American sweetgum ground truth area. The LiDAR closely matches the hand held photo captured above. The photo mainly encompasses American sweetgum trees; however a willow oak and a pine species are visible in the handheld image.
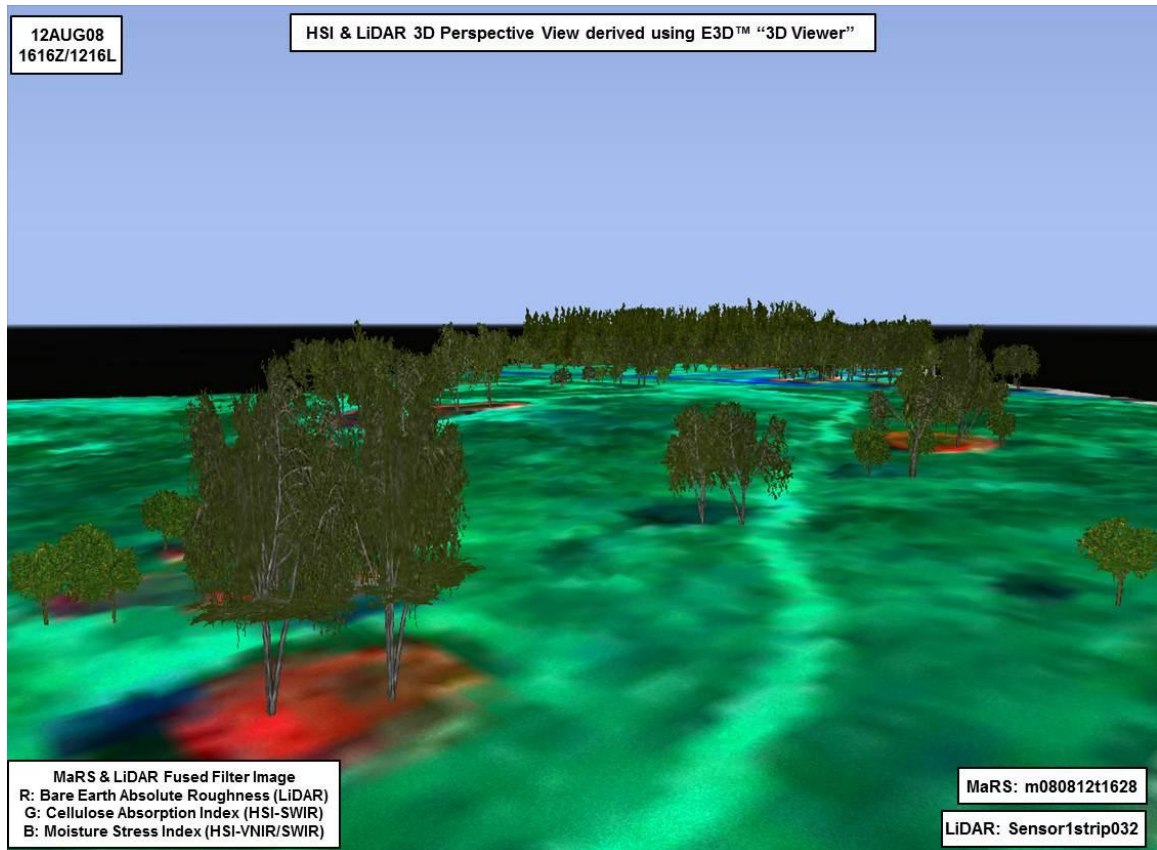
Figure 29: HSI and LiDAR 3D perspective view of the trails area. It is important to note here that the color presented over top the LiDAR is a fused HSI and LiDAR color image. The same color combination was used in Figure 18. This particular color filter and transformation image combination clearly shows the location of the trail through the Arboretum.

REFERENCES

REFERENCES

[1] Abrams, M.J., Ashley, R.P., Rowan, L.C., Goetz, A.F.H., and Kahle, A.B., "Mapping of hydrothermal alteration in the Cuprite mining district, Nevada using aircraft scanner images for the spectral region 0.46-2.36 μm," Geology, v. 5, p. 713-718 (1977).

[2] Applied Imagery Copyright © 2011. URL: http://www.appliedimagery.com

[3] Asner, G.P. and Lobell, D.B., "A Biogeophysical Approach for Automated SWIR Unmixing of Soils and Vegetation," Remote Sensing of The Environment, V. 74, 99–112 (2000).

[4] Asner, G.P., Knapp, D.E., Kennedy-Bowdoin, T., Jones, M.O., Martin, R.E., Boardman, J., Hughes, R. F., "Invasive species detection in Hawaiian rainforests using airborne imaging spectroscopy and LiDAR," Remote Sensing of The Environment 112:1942-1955 (2008).

[5] Asner, G.P., Knapp, D.E., Kennedy-Bowdoin, T., Jones, M.O., Martin, R.E., Boardman, J., Field, C.B., "Carnegie Airborne Observatory: in-flight fusion of hyperspectral imaging and waveform light detection and ranging (wLiDAR) for three-dimensional studies of ecosystems," Journal of Applied Remote Sensing, Vol. 1, 013536, 1-21 (2007).

[6] "The Benefits of the 8 Spectral Bands of WorldView-2," Digital Globe [white paper] (2009). URL: http://worldview2.digitalglobe.com/docs/WorldView-2_8-Band_Applications_Whitepaper.pdf

[7] BCAL LiDAR Tools ver 1.4.2. Idaho State University, Department of Geosciences, Boise Center Aerospace Laboratory (BCAL), Boise, Idaho. URL: http://bcal.geology.isu.edu/tools-2/envi-tools

[8] Bernstein, L.S., Adler-Golden, S.M., Ratkowski, A.J., "In-scene-based atmospheric correction of uncalibrated VISible-SWIR (VIS-SWIR) hyper- and multispectral imagery," in SPIE proceedings, Europe Security and Defense, Remote Sensing, V. 7107 (2008).

[9] Boardman, J.W., and Kruse, F.A., "Mapping target signatures via partial unmixing of AVIRIS data: in Summaries, Fifth JPL Airborne Earth Science Workshop, JPL Publication 95-1, v. 1, p. 23 – 26.

[10] Boardman, J.W., "Leveraging the high dimensionality of AVIRIS data for improved sub-pixel target unmixing and rejection of false positives: mixture tuned matched filtering," In: 7th JPL Airborne Geoscience Workshop, pp. 55-56 (1998).

[11] Bradley, A.P., "The use of the area under the ROC Curve in the evaluation of machine learning algorithms," *Pattern Recognition*, V. 30, No.7, pp 1145-1159 (1997).

[12] Brook, A., Ben-Dor, E., Richter, R., "Fusion of Hyperspectral Images and LiDAR Data for Civil Engineering Structure Monitoring," in Hyperspectral 2010 Workshop Proceedings (2010).

[13] Ceccato, P., Flasse, S. Tarantola, Jacquemoud, S. and Gregoire, J.M., "Detecting Vegetation Leaf Water Content Using Reflectance in the Optical Domain," Remote Sensing of Environment V. 77, Pgs. 22-33 (2001).

[14] Dalponte, M., Bruzzone, L., Gianelle, D., "Fusion of Hyperspectral and LIDAR Remote Sensing Data for Classification of Complex Forest Areas," IEEE Transactions on Geoscience and Remote Sensing, Vol. 46, No. 5, 1416-1427 (2009).

[15] Daughtry, C.S.T., Hunt, E.R. Jr., and McMurtrey, E.R. III., "Assessing Crop Residue Cover Using Shortwave Infrared Reflectance," Remote Sensing of Environment V. 90, Pgs. 126-134 (2004).

[16] ESRI 2012. ArcGIS Desktop: Release 10. Redlands, CA: Environmental Systems Research Institute. URL: http://www.esri.com

[17] Evans, J.S., Hudak, A.T., Faux, R., Smith, A.M.S., "Discrete Return Lidar in Natural Resources: Recommendations for Project Planning, Data Processing, and Deliverables." Remote Sensing. 1(4):776-794 (2009).

[18] Exelis Visual Information Solutions. Copyright © 2012. Boulder, Colorado. URL: http://www.exelisvis.com/language/en-US/ProductsServices/ENVI.aspx

[19] Exelis Visual Information Solutions, "Vegetation Indices," ENVI® 5.0 Help Files. Boulder, Colorado: Exelis Visual Information Solutions (2012).

[20] Geerling, G.W., Labrador-Garcia, M., Clevers, J.P.G.W., Ragas, A.M.J., Smits, A.J.M., "Classification of floodplain vegetation by data fusion of spectral (CASI) and LiDAR data," International Journal of Remote Sensing, 28:19, 4263 - 4284 (2007).

[21] Goetz, A.F.H., Vane, G., Solomon, J.E., Rock, B.N., "Imaging spectrometry for earth remote-sensing," Science, V. 228, 1147–1153 (1985).

[22] Hackwell, J.A., Warren, D.W., Bongiovi, R.P., Hansel, S.J., Hayhurst, T.L., Mabry, D.J., Sivjee, M.G., & Skinner, J.W., "LWIR/ MWIR imaging hyperspectral sensor for airborne and ground-based remote sensing," SPIE, 2819, 102– 107 (1996).

[23] Hall, R.K., Watkins, R.L., Heggem, D.T., Jones, K.B., Kaufman, P.R., Moore, S.B., Gregory, S.J., "Quantifying structural physical habitat attributes using LiDAR and hyperspectral imagery," Environmental Monitoring and Assessment 159:63-83 (2009).

[24] Jackson, T.L., Chen, D.M., Cosh, F.L., Anderson, M.C., Doriaswamy, W.P., and Hunt, E.R., "Vegetation Water Content Mapping Using Landsat Data Derived Normalized Difference Water Index for Corn and Soybeans," Remote Sensing of Environment V. 92, Pgs. 475-482 (2004).

[25] Jones, T.G., Coops, N.C., Sharma, T., "Assessing the utility of airborne hyperspectral and LiDAR data for species distribution mapping in the coastal Pacific Northwest, Canada," Remote Sensing of Environment, V. 114, 2841-2852 (2010).

[26] Kaufman, Y.J. and Tanre, D., "Strategy for Direct and Indirect Methods for Correcting the Aerosol Effect on Remote Sensing: from AVHRR to EOS-MODIS," Remote Sensing of Environment V. 55, Pgs. 65-79 (1996).

[27] Koetz, B., Morsdorf, F., van der Linden, S., Curt, T., Allgöwer, B., "Multi-source land cover classification for forest fire management based on imaging spectrometry and LiDAR data," Forest Ecology and Management, V. 256, 263-271 (2008).

[28] Kraut, S., Scharf, L. L., and Butler, R.W., "The adaptive coherence estimator: a uniformly most-powerful-invariant adaptive detection statistic," IEEE Trans. on Signal Processing, vol. 53, no. 2, pp. 427-438 (2005).

[29] Kruse, F.A., "Use of Airborne Imaging Spectrometer Data to Map Minerals Associated with Hydrothermally Altered Rocks in the Northern Grapevine Mountains, Nevada, and California," Remote Sensing of The Environment. V. 24, 31 - 51 (1988).

[30] Li, W., Guo, Q., Jakubowski, M.K., Kelly, M., "A New Method for Segmenting Individual Trees from the Lidar Point Cloud," Photogrammetric Engineering & Remote Sensing, Vol. 78, No. 1, 75-84 (2012).

[31] Mundt, J.T., Streuker, D.R., Glenn, N.F., "Mapping Sagebrush Distribution Using Fusion of Hyperspectral and Lidar Classifications," Photogrammetric Engineering & Remote Sensing ,Vol. 72, No. 1. 47–54 (2006).

[32] Onojeghuo, A.O., and Blackburn, G.A., "Optimising the use of hyperspectral and LiDAR data for mapping reedbed habitats," Remote Sensing of the Environment. V. 115, 2025 – 2034 (2011).

[33] Overwatch Systems, Ltd, Copyright © 2012. All Rights Reserved. Overwatch Systems, Ltd. is an indirect wholly owned subsidiary of Textron Inc. URL: http://www.overwatch.com/products/remote_view_pro.php

[34] Penuelas, J., Baret, F., and Filella, I., "Semi-Empirical Indices to Assess Carotenoids/Chlorophyll-a Ratio from Leaf Spectral Reflectance," Photosynthetica V. 31, Pgs. 221-230 (1995).

[35] Pohl, C. and van Genderen, J.L., "Multisensor image fusion in remote sensing: concepts, methods and applications," International Journal of Remote Sensing, vol. 19, no. 5, 823-854 (1998).

[36] Ribeiro da Luz, B., and Crowley, J.K., "Identification of plant species by using high spatial and spectral resolution thermal infrared (8.0–13.5 μm) imagery," Remote Sensing of Environment, V. 114 Pgs. 404-413 (2010).

[37] Rouse, J.W., Haas, R.H., Schell, J.A., and Deering, D.W., "Monitoring Vegetation Systems in the Great Plains with ERTS," In the Third ERTS Symposium, NASA SP-351 I: 309-317 (1973).

[38] Salvador, M.Z., and Resmini, R.G., "Comparison of spectral matching techniques for vegetation species delineation of the National Arboretum," in SPIE Proceedings, Algorithms and Technologies for Multispectral, Hyperspectral, and Ultraspectral Imagery XV (2009).

[39] Sankee, T., and Glenn, N., "Landsat-5 TM and LiDAR Fusion for Sub-pixel Juniper Tree Cover Estimates in a Western Rangeland," Photogrammetric Engineering & Remote Sensing. V. 77. No. 12. Pgs. 1241 – 1248 (2011).

[40] Schmidt, K.S., and Skidmore, A.K., "Spectral discrimination of vegetation types in a coastal wetland," Remote Sensing of The Environment, V. 85 Pgs. 92-108 (2002).

[41] Schowengerdt, R. A., "Remote Sensing: Models and Methods for Image Processing," Academic Press (1997).

[42] Simi, C., and Reith, E., "The Mapping Reflected-energy Sensor–MaRS: A New Level of Hyperspectral Technology," in SPIE Proceedings, Imaging Spectrometry XIV (2009).

[43] Streutker, D. and Glenn, N., "LiDAR measurement of sagebrush steppe vegetation heights," Remote Sensing of Environment, V. 102, Pgs. 135-145 (2006).

[44] Teillet, P.M., "Image correction for radiometric effects in remote sensing," International Journal Remote Sensing. V. 7. Pgs. 1637 – 1651 (1986).

[45] USGS Orthoimagery. Obtained from the *National Map Viewer.* URL: http://cumulus.cr.usgs.gov/

[46] Vaughan, R.G., Calvin, W.M., Taranik, J.V., "SEBASS hyperspectral thermal infrared data: surface emissivity measurement and mineral mapping," Remote Sensing of Environment. V. 85, 48 – 63 (2003).

[47] Vogelmann, J.E., Rock, B.N., and Moss, D.M., "Red Edge Spectral Measurements from Sugar Maple Leaves," International Journal of Remote Sensing V. 14 Pgs. 1563-1575 (1993).

[48] Wehr, A. and Lohr, U., "Airborne laser scanning—an introduction and overview," ISPRS Journal of Photogrammetry and Remote Sensing, V. 54, 68–82 (1999).

[49] West, M.S. and Resmini, R.G., "Hyperspectral imagery and LiDAR for Geological Analysis of Cuprite, Nevada" in SPIE Proceedings, Algorithms and Technologies for Multispectral, Hyperspectral, and Ultraspectral Imagery XV (2009).

CURRICULUM VITAE

Joshua F. Magarick graduated from the Friends School of Baltimore, in 2000. He received his Bachelor of Arts from the University of Colorado at Boulder in 2004. He has been employed with the National Geospatial-Intelligence Agency for over 7 years.